

A SPHERICAL ANALYSIS OF ADAM WITH BATCH NORMALIZATION

Simon Roburin*

LIGM (UMR 8049), École des Ponts, UPE
valeo.ai

Yann de Mont-Marin*

Département d'informatique de l'ENS, PSL
Inria

Andrei Bursuc

valeo.ai

Renaud Marlet

valeo.ai

Patrick Pérez

valeo.ai

Mathieu Aubry

LIGM (UMR 8049), École des Ponts, UPE

Batch Normalization (BN) is a prominent deep learning technique. In spite of its apparent simplicity, its implications over optimization are yet to be fully understood. While previous studies mostly focus on the interaction between BN and stochastic gradient descent (SGD), we develop a geometric perspective which allows us to precisely characterize the relation between BN and Adam. More precisely, we leverage the radial invariance of groups of parameters, such as filters for convolutional neural networks, to translate the optimization steps on the L_2 unit hypersphere. This formulation and the associated geometric interpretation shed new light on the training dynamics. Firstly, we use it to derive the first effective learning rate expression of Adam. Then we show that, in the presence of BN layers, performing SGD alone is actually equivalent to a variant of Adam constrained to the unit hypersphere. Finally, our analysis outlines phenomena that previous variants of Adam act on and we experimentally validate their importance in the optimization process.

1 INTRODUCTION

The optimization process of deep neural networks is still poorly understood. Their training involves minimizing a high-dimensional non-convex function, which has been proved to be a NP-hard problem (Blum & Rivest, 1989). Yet, elementary gradient-based methods show good results in practice. To improve the quality of reached minima, numerous methods have stemmed in the last years and become common practices. One of the most prominent is Batch Normalization (BN) (Ioffe & Szegedy, 2015), which improves significantly both the optimization stability and the prediction performance; it is now used in most deep learning architectures. However, the interaction of BN with optimization and its link to regularization remain open research topics. Previous studies highlighted mechanisms of the interaction between BN and SGD, both empirically (Santurkar et al., 2018) and theoretically (Arora et al., 2019; Bjorck et al., 2018; Hoffer et al., 2018b). None of them studied the interaction between BN and one of the most common adaptive schemes for Neural Networks (NN), Adam (Kingma & Ba, 2015), except van Laarhoven (2017), which tackled it only in the asymptotic regime. In this work, we provide an extensive analysis of the relation between BN and Adam during the whole training procedure.

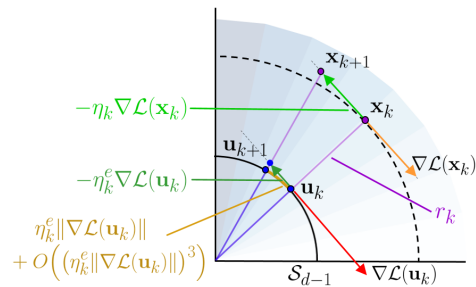


Figure 1: **Illustration of the spherical perspective for SGD.** The loss function \mathcal{L} of a NN w.r.t. the parameters $\mathbf{x}_k \in \mathbb{R}^d$ of a neuron followed by a BN is radially invariant. The neuron update $\mathbf{x}_k \rightarrow \mathbf{x}_{k+1}$ in the original space, with velocity $\eta_k \nabla \mathcal{L}(\mathbf{x}_k)$, corresponds to an update $\mathbf{u}_k \rightarrow \mathbf{u}_{k+1}$ of its projection through an exponential map on the unit hypersphere S_{d-1} with velocity $\eta_k^e \|\nabla \mathcal{L}(\mathbf{u}_k)\|$ at order 2 (see details in Section 2.3).

*Equal contribution

One of the key effects of BN is to make NNs invariant to positive scalings of groups of parameters. The core idea of this paper is precisely to focus on these groups of radially-invariant parameters and analyze their optimization projected on the L_2 unit hypersphere (see Fig. 1), which is topologically equivalent to the quotient manifold of the parameter space by the scaling action. One could directly optimize parameters on the hypersphere as Cho & Lee (2017), yet, most optimization methods are still performed successfully in the original parameter space. Here we propose to study an optimization scheme for a given group of radially-invariant parameters through its image scheme on the unit hypersphere. This geometric perspective sheds light on the interaction between normalization layers and Adam, and also highlights an interesting link between standard SGD and Adam. We believe this kind of analysis is an important step towards a better understanding of the effect of BN on NN optimization, which would also include layer interaction. Please note that, although our discussion and experiments focus on BN, our analysis could be applied to any radially-invariant model.

The paper is organized as follows. In **Section 2**, we introduce our spherical framework to study the optimization of radially-invariant models. We also define a generic optimization scheme that encompasses methods such as SGD with momentum (SGD-M) and Adam. We then derive its image step on the unit hypersphere, leading to definitions and expressions of *effective learning rate* and *effective learning direction*. This new definition is explicit and has a clear interpretation, whereas the definition of van Laarhoven (2017) is asymptotic and the definitions of Arora et al. (2019) and of Hoffer et al. (2018b) are variational. In **Section 3**, we leverage the tools of our spherical framework to link theoretically SGD and Adam. We show that, in presence of BN layers, SGD behaves like Adam without momentum, adapted and constrained to the hypersphere. In **Section 4**, we analyze the effective learning direction for Adam. The spherical framework highlights phenomena that previous variants of Adam (Loshchilov & Hutter, 2017; Cho & Lee, 2017) act on. We perform an empirical study of these phenomena and show that they play a significant role in the training of convolutional neural networks (CNNs). In **Section 5**, these results are put in perspective with related work.

Our main contributions are the following:

- A framework to analyze and compare order-1 optimization schemes of radially-invariant models;
- The first explicit expression of the effective learning rate for Adam;
- The demonstration that, in the presence of BN layers, standard SGD behaves like Adam without momentum, constrained and adapted to the unit hypersphere;
- The identification and study of geometrical phenomena that occur with Adam and impact significantly the training of CNNs with BN.

2 SPHERICAL FRAMEWORK AND EFFECTIVE LEARNING RATE

In this section, we provide background on radial invariance and introduce a generic optimization scheme. Projecting the scheme update on the unit hypersphere leads to the formal definitions of effective learning rate and learning direction. This geometric perspective leads to the first explicit expression of the effective learning rate for Adam. The main notations are summarized in Figure 1.

2.1 RADIAL INVARIANCE

We consider a family of parametric functions $\phi_{\mathbf{x}} : \mathbb{R}^{in} \rightarrow \mathbb{R}^{out}$ parameterized by a group of radially-invariant parameters $\mathbf{x} \in \mathbb{R}^d \setminus \{\mathbf{0}\}$, i.e., $\forall \rho > 0, \phi_{\rho\mathbf{x}} = \phi_{\mathbf{x}}$ (possible other parameters of $\phi_{\mathbf{x}}$ are omitted for clarity), a dataset $\mathcal{D} \subset \mathbb{R}^{in} \times \mathbb{R}^{out}$, a loss function $\ell : \mathbb{R}^{out} \times \mathbb{R}^{out} \rightarrow \mathbb{R}$ and a training loss function $\mathcal{L} : \mathbb{R}^d \rightarrow \mathbb{R}$ defined as:

$$\mathcal{L}(\mathbf{x}) \stackrel{\text{def}}{=} \frac{1}{|\mathcal{D}|} \sum_{(\mathbf{s}, \mathbf{t}) \in \mathcal{D}} \ell(\phi_{\mathbf{x}}(\mathbf{s}), \mathbf{t}). \quad (1)$$

It verifies: $\forall \rho > 0, \mathcal{L}(\rho\mathbf{x}) = \mathcal{L}(\mathbf{x})$. In the context of NNs, the group of radially-invariant parameters \mathbf{x} can be the parameters of a single neuron in a linear layer or the parameters of a whole filter in a convolutional layer, followed by BN (see Appendix A for details, and Appendix B for the application to other normalization schemes such as InstanceNorm (Ulyanov et al., 2016), LayerNorm (Ba et al., 2016) or GroupNorm (Wu & He, 2018)).

The quotient of the parameter space by the equivalence relation associated to radial invariance is topologically equivalent to a sphere. We consider here the L_2 sphere $\mathcal{S}_{d-1} = \{\mathbf{u} \in \mathbb{R}^d / \|\mathbf{u}\|_2 = 1\}$

whose canonical metric corresponds to angles: $d_S(\mathbf{u}_1, \mathbf{u}_2) = \arccos(\langle \mathbf{u}_1, \mathbf{u}_2 \rangle)$. This choice of metric is relevant to study NNs since filters in CNNs or neurons in MLPs are applied through scalar product to input data. Besides, normalization in BN layers is also performed using the L_2 norm.

Our framework relies on the decomposition of vectors into radial and tangential components. During optimization, we write the radially-invariant parameters at step $k \geq 0$ as $\mathbf{x}_k = r_k \mathbf{u}_k$ where $r_k = \|\mathbf{x}_k\|$ and $\mathbf{u}_k = \mathbf{x}_k / \|\mathbf{x}_k\|$. For any quantity $\mathbf{q}_k \in \mathbb{R}^d$ at step k , we write $\mathbf{q}_k^\perp = \mathbf{q}_k - \langle \mathbf{q}_k, \mathbf{u}_k \rangle \mathbf{u}_k$ its tangential component relatively to the current direction \mathbf{u}_k .

The following lemma states that the gradient of a radially-invariant loss function is tangential and -1 homogeneous:

Lemma 1 (Gradient of a function with radial invariance). *If $\mathcal{L} : \mathbb{R}^d \rightarrow \mathbb{R}$ is radially invariant and almost everywhere differentiable, then, for all $\rho > 0$ and all $\mathbf{x} \in \mathbb{R}^d$ where \mathcal{L} is differentiable:*

$$\langle \nabla \mathcal{L}(\mathbf{x}), \mathbf{x} \rangle = 0 \quad \text{and} \quad \nabla \mathcal{L}(\mathbf{x}) = \rho \nabla \mathcal{L}(\rho \mathbf{x}). \quad (2)$$

2.2 GENERIC OPTIMIZATION SCHEME

There is a large body of literature on optimization schemes (Sutskever et al., 2013; Duchi et al., 2011; Tieleman & Hinton, 2012; Kingma & Ba, 2015; Loshchilov & Hutter, 2019). We focus here on two of the most popular ones, namely SGD and Adam (Kingma & Ba, 2015). Yet, to establish general results that may apply to a variety of other schemes, we introduce here a *generic optimization update*:

$$\mathbf{x}_{k+1} = \mathbf{x}_k - \eta_k \mathbf{a}_k \oslash \mathbf{b}_k, \quad (3)$$

$$\mathbf{a}_k = \beta \mathbf{a}_{k-1} + \nabla \mathcal{L}(\mathbf{x}_k) + \lambda \mathbf{x}_k, \quad (4)$$

where $\mathbf{x}_k \in \mathbb{R}^d$ is the group of radially-invariant parameters at iteration k , \mathcal{L} is the group's loss estimated on a batch of input data, $\mathbf{a}_k \in \mathbb{R}^d$ is a momentum, $\mathbf{b}_k \in \mathbb{R}^d$ is a division vector that can depend on the trajectory $(\mathbf{x}_i, \nabla \mathcal{L}(\mathbf{x}_i))_{i \in [0, k]}$, $\eta_k \in \mathbb{R}$ is the scheduled trajectory-independent learning rate, \oslash denotes the Hadamard element-wise division, β is the momentum parameter, and λ is the L_2 -regularization parameter. We show how it encompasses several known optimization schemes.

Stochastic gradient descent (SGD) has proven to be an effective optimization method in deep learning. It can include L_2 regularization (also called weight decay) and momentum. Its updates are:

$$\mathbf{x}_{k+1} = \mathbf{x}_k - \eta_k \mathbf{m}_k, \quad (5)$$

$$\mathbf{m}_k = \beta \mathbf{m}_{k-1} + \nabla \mathcal{L}(\mathbf{x}_k) + \lambda \mathbf{x}_k, \quad (6)$$

where \mathbf{m}_k is the momentum, β is the momentum parameter, and λ is the L_2 -regularization parameter. It corresponds to our generic scheme (Eqs. 3-4) with $\mathbf{a}_k = \mathbf{m}_k$ and $\mathbf{b}_k = [1 \cdots 1]^\top$.

Adam is likely the most common adaptive scheme for NNs. Its updates are:

$$\mathbf{x}_{k+1} = \mathbf{x}_k - \eta_k \frac{\mathbf{m}_k}{1 - \beta_1^{k+1}} \oslash \sqrt{\frac{\mathbf{v}_k}{1 - \beta_2^{k+1}} + \epsilon}, \quad (7)$$

$$\mathbf{m}_k = \beta_1 \mathbf{m}_{k-1} + (1 - \beta_1)(\nabla \mathcal{L}(\mathbf{x}_k) + \lambda \mathbf{x}_k), \quad \mathbf{v}_k = \beta_2 \mathbf{v}_{k-1} + (1 - \beta_2)(\nabla \mathcal{L}(\mathbf{x}_k) + \lambda \mathbf{x}_k)^2, \quad (8)$$

where \mathbf{m}_k is the momentum with parameter β_1 , \mathbf{v}_k is the second-order moment with parameter β_2 , and ϵ prevents division by zero. (Here and in the following, the square and the square root of a vector are to be understood as element-wise.) It corresponds to our generic scheme (Eqs. 3-4) with $\beta = \beta_1$ and:

$$\mathbf{a}_k = \frac{\mathbf{m}_k}{1 - \beta_1}, \quad \mathbf{b}_k = \frac{1 - \beta_1^{k+1}}{1 - \beta_1} \sqrt{\frac{\mathbf{v}_k}{1 - \beta_2^{k+1}} + \epsilon}. \quad (9)$$

2.3 IMAGE OPTIMIZATION ON THE HYPERSPHERE

The radial invariance implies that the radial part of the parameter update \mathbf{x} does not change the function $\phi_{\mathbf{x}}$ encoded by the model, nor does it change the loss $\mathcal{L}(\mathbf{x})$. To understand optimization in this context, we need to separate the quantities that can (tangential part) and cannot (radial part) change the loss function. Theorem 2 formulates the spherical decomposition (Eqs. 3-4) in simple terms. It relates the update of radially-invariant parameters in the parameter space \mathbb{R}^d and their update on \mathcal{S}_{d-1} through an exponential map.

Theorem 2 (Image step on \mathcal{S}_{d-1}). *The update of a group of radially-invariant parameters \mathbf{x}_k at step k corresponds to an update of its projection \mathbf{u}_k on \mathcal{S}_{d-1} through an exponential map at \mathbf{u}_k with velocity $\eta_k^e \mathbf{c}_k^\perp$, at order 3:*

$$\mathbf{u}_{k+1} = \text{Exp}_{\mathbf{u}_k} \left(- \left[1 + O \left((\eta_k^e \|\mathbf{c}_k^\perp\|)^2 \right) \right] \eta_k^e \mathbf{c}_k^\perp \right), \quad (10)$$

where $\text{Exp}_{\mathbf{u}_k}$ is the exponential map on \mathcal{S}_{d-1} , and with

$$\mathbf{c}_k \stackrel{\text{def}}{=} r_k \mathbf{a}_k \oslash \frac{\mathbf{b}_k}{d^{-1/2} \|\mathbf{b}_k\|}, \quad \eta_k^e \stackrel{\text{def}}{=} \frac{\eta_k}{r_k^2 d^{-1/2} \|\mathbf{b}_k\|} \left(1 - \frac{\eta_k \langle \mathbf{c}_k, \mathbf{u}_k \rangle}{r_k^2 d^{-1/2} \|\mathbf{b}_k\|} \right)^{-1}. \quad (11)$$

More precisely:

$$\mathbf{u}_{k+1} = \frac{\mathbf{u}_k - \eta_k^e \mathbf{c}_k^\perp}{\sqrt{1 + (\eta_k^e \|\mathbf{c}_k^\perp\|)^2}}. \quad (12)$$

The proof is given in Appendix C.1.1 and the theorem is illustrated in the case of SGD in Figure 1. Note that with typical values in CNN training we have $1 - \frac{\eta_k \langle \mathbf{c}_k, \mathbf{u}_k \rangle}{r_k^2 d^{-1/2} \|\mathbf{b}_k\|} > 0$, which is a property needed for the proof. Another hypothesis is that steps on the hypersphere are shorter than π . These hypotheses are discussed and empirically verified in Appendix C.1.2.

2.4 EFFECTIVE LEARNING RATE FOR ADAM

In Theorem 2, the normalized parameters update in Eq. 10 can be read $\mathbf{u}_{k+1} \approx \text{Exp}_{\mathbf{u}_k} (-\eta_k^e \mathbf{c}_k^\perp)$, where η_k^e and \mathbf{c}_k^\perp can then be respectively interpreted as the learning rate and the direction of an optimization step constrained to \mathcal{S}_{d-1} since \mathbf{a}_k is the momentum and, with Lemma 1, the quantity $r_k \mathbf{a}_k$ in \mathbf{c}_k can be seen as *a momentum on the hypersphere*. Due to the radial invariance, only the change of parameter on the unit hypersphere corresponds to a change of model function. Hence we can interpret η_k^e and \mathbf{c}_k^\perp as *effective learning rate* and *effective learning direction*. In other words, these quantities correspond to the learning rate and direction on the hypersphere that reproduce the function update of the optimization step.

Using Theorem 2, we can derive actual effective learning rates for any optimization scheme that fits our generic framework. These expressions, summarized in Table 1 are explicit and have a clear interpretation, in contrast to learning rates in (van Laarhoven, 2017), which are approximate and asymptotic, and in (Hoffer et al., 2018a; Arora et al., 2019), which are variational and restricted to SGD without momentum only.

In particular, we provide the first explicit expression of the effective learning rate for Adam:

$$\eta_k^e = \frac{\eta_k}{r \nu_k} \left(1 - \frac{\eta_k \langle \mathbf{c}_k, \mathbf{u}_k \rangle}{r \nu_k} \right)^{-1} \quad (13)$$

where $\nu_k = r_k d^{-1/2} \|\mathbf{b}_k\|$ is homogeneous to the norm of a gradient on the hypersphere and can be related to an *second-order moment on the hypersphere* (see Appendix.C.1.3 for details). This notation also simplifies the in-depth analysis in Section 4, allowing a better interpretation of formulas.

The expression of the effective learning rate of Adam, i.e., the amplitude of the step taken on the hypersphere, reveals a dependence on the dimension d (through ν) of the considered group of radially-invariant parameters. In the case of an MLP or CNN that stacks layers with neurons or filters of different dimensions, the learning rate is thus tuned differently from one layer to another.

We can also see that for all schemes the learning rate is tuned by the dynamics of radiuses r_k , which follow:

$$\frac{r_{k+1}}{r_k} = \left(1 - \frac{\eta_k \langle \mathbf{c}_k, \mathbf{u}_k \rangle}{r_k^2 d^{-1/2} \|\mathbf{b}_k\|} \right) \sqrt{1 + (\eta_k^e \|\mathbf{c}_k^\perp\|)^2}. \quad (14)$$

In contrast to previous studies (Arora et al., 2019; van Laarhoven, 2017), this result demonstrates that for momentum methods, $\langle \mathbf{c}_k, \mathbf{u}_k \rangle$, which involves accumulated gradients terms in the momentum as well as L_2 regularization, tunes the learning rate (*cf.* Fig.1).

Table 1: Effective learning rate and direction for optimization schemes (k omitted), with $\nu = r d^{-1/2} \|\mathbf{b}\|$.

Scheme	η^e	\mathbf{c}^\perp
SGD	$\frac{\eta}{r^2}$	$\nabla \mathcal{L}(\mathbf{u})$
SGD + L_2	$\frac{\eta}{r^2(1-\eta\lambda)}$	$\nabla \mathcal{L}(\mathbf{u})$
SGD-M	$\frac{\eta}{r^2} \left(1 - \frac{\eta \langle \mathbf{c}, \mathbf{u} \rangle}{r^2} \right)^{-1}$	\mathbf{c}^\perp
Adam	$\frac{\eta}{r\nu} \left(1 - \frac{\eta \langle \mathbf{c}, \mathbf{u} \rangle}{r\nu} \right)^{-1}$	\mathbf{c}^\perp

3 SGD IS A VARIATION OF ADAM ON THE HYPERSPHERE

We leverage the tools introduced in the spherical framework to find a scheme constrained to the hypersphere that is equivalent to SGD. We show that for radially-invariant models, SGD behaves like Adam without momentum, adapted and constrained to the unit hypersphere.

3.1 EQUIVALENCE BETWEEN TWO OPTIMIZATION SCHEMES

Due to the radial invariance, the functional space of the model is encoded by \mathcal{S}_{d-1} . In other words, two schemes with the same sequence of groups of radially-invariant parameters on the hypersphere $(\mathbf{u}_k)_{k \geq 0}$ encode the same sequence of model functions. Two optimization schemes S and \tilde{S} are equivalent iff $\forall k \geq 0, \mathbf{u}_k = \tilde{\mathbf{u}}_k$. By using Eq. 12, we obtain the following lemma, which is useful to prove the equivalence of two given optimization schemes:

Lemma 3 (Sufficient condition for the equivalence of optimization schemes).

$$\begin{cases} \mathbf{u}_0 = \tilde{\mathbf{u}}_0 \\ \forall k \geq 0, \eta_k^e = \tilde{\eta}_k^e, \mathbf{c}_k^\perp = \tilde{\mathbf{c}}_k^\perp \end{cases} \Rightarrow \forall k \geq 0, \mathbf{u}_k = \tilde{\mathbf{u}}_k. \quad (15)$$

3.2 A HYPERSPHERE-CONSTRAINED SCHEME EQUIVALENT TO SGD

We now study, within our spherical framework, SGD with L_2 regularization, i.e., the update $\mathbf{x}_{k+1} = \mathbf{x}_k - \eta_k(\nabla \mathcal{L}(\mathbf{x}_k) - \lambda_k \mathbf{x}_k)$. We know that SGD yields an adaptive behaviour because it is scheduled by the radius dynamic, which depends on gradients. In fact, the tools in our framework allow us to find a scheme constrained to the unit hypersphere that is equivalent to SGD: a variant of AdamG (Cho & Lee, 2017), which itself is an adaptation of Adam constrained to the hypersphere. Dubbed AdamG*, this equivalent scheme corresponds to the case of a null momentum factor $\beta_1 = 0$, an non-null initial second-order moment v_0 , an offset of the scalar second-order moment $k+1 \rightarrow k$ and the absence of the bias correction term $1 - \beta_2^{k+1}$:

$$\text{(AdamG*)} : \begin{cases} \hat{\mathbf{x}}_{k+1} = \mathbf{x}_k - \eta_k \frac{\nabla \mathcal{L}(\mathbf{x}_k)}{\sqrt{v_k}}, \\ \mathbf{x}_{k+1} = \frac{\hat{\mathbf{x}}_{k+1}}{\|\hat{\mathbf{x}}_{k+1}\|}, \\ v_{k+1} = \beta v_k + \|\nabla \mathcal{L}(\mathbf{x}_k)\|^2. \end{cases}$$

Starting from SGD, we first use Lemma 3 to find an equivalence scheme with simpler radius dynamic. We resolve this radius dynamic with a Taylor expansion at order 2 in $(\eta_k \|\nabla \mathcal{L}(\mathbf{u}_k)\|)^2 / r_k^2$. A second use of Lemma 3 finally leads to the following scheme equivalence in Theorem 4 (see proof in Appendix C.1.4). If we call « equivalent at order 2 in the step » a scheme equivalence that holds when we use for r_k an expression that satisfies the radius dynamic with a Taylor expansion at order 2 we have the following theorem:

Theorem 4 (SGD equivalent scheme on the unit hypersphere). *For any $\lambda > 0, \eta > 0, r_0 > 0$, we have the following equivalence when using the radius dynamic at order 2 in $(\eta_k \|\nabla \mathcal{L}(\mathbf{u}_k)\|)^2 / r_k^2$:*

$$\begin{cases} \text{(SGD)} \\ \mathbf{x}_0 = r_0 \mathbf{u}_0 \\ \lambda_k = \lambda \\ \eta_k = \eta \end{cases} \text{ is scheme-equivalent at order 2 in step with } \begin{cases} \text{(AdamG*)} \\ \mathbf{x}_0 = \mathbf{u}_0 \\ \beta = (1 - \eta\lambda)^4 \\ \eta_k = (2\beta)^{-1/2} \\ v_0 = r_0^4 (2\eta^2 \beta^{1/2})^{-1}. \end{cases}$$

The notion of scheme equivalence offers a precise analysis of SGD for radially-invariant parameters and highlights a rather unexpected link with Adam. The scheduling performed by the radius dynamics actually replicates the effect of dividing the learning rate by the second-order moment of the gradient norm: v_k . In other words, training CNNs with BN makes SGD an adaptive scheme on the unit hypersphere, which is enough to represent the functional space encoded by the network.

4 GEOMETRIC PHENOMENA IN ADAM

Our framework with its geometrical interpretation reveals intriguing behaviors occurring in Adam. The unit hypersphere is enough to represent the functional space encoded by the network. From the

perspective of manifold optimization, the optimization direction would only depend on the trajectory on that manifold. In the case of Adam, the effective direction not only depends on the trajectory on the hypersphere but also on the deformed gradients and additional radial terms. These terms are thus likely to play a role in Adam optimization.

In order to understand their role, we describe these geometrical phenomena in Section 4.1. Interestingly, previous variants of Adam, AdamW (Loshchilov & Hutter, 2017) and AdamG (Cho & Lee, 2017) are related to these phenomena. To study empirically their importance, we consider in Section 4.2 variants of Adam that first provide a direction intrinsic to the unit hypersphere, without deformation of the gradients, and then where radial terms are decoupled from the direction. The empirical study of these variants over a variety of datasets and architectures suggests that these behaviors do play a significant role in CNNs training with BN.

4.1 IDENTIFICATION OF GEOMETRICAL PHENOMENA IN ADAM

Here, we perform an in-depth analysis of the effective learning direction of Adam.

(a) Deformed gradients. Considering the quantities defined for a generic scheme in Eq. 11, \mathbf{b}_k has a deformation effect on \mathbf{a}_k , due to the Hadamard division by $\frac{\mathbf{b}_k}{d^{-1/2}\|\mathbf{b}_k\|}$, and a scheduling effect $d^{-1/2}\|\mathbf{b}_k\|$ on the effective learning rate. In the case where the momentum factor is null $\beta_1 = 0$, the direction of the update at step k is $\nabla\mathcal{L}(\mathbf{u}_k) \otimes \frac{\mathbf{b}_k}{d^{-1/2}\|\mathbf{b}_k\|}$ (Eq. 11) and the deformation $\frac{\mathbf{b}_k}{d^{-1/2}\|\mathbf{b}_k\|}$ may push the direction of the update outside the tangent space of \mathcal{S}_{d-1} at \mathbf{u}_k , whereas the gradient itself lies in the tangent space. This deformation is in fact not isotropic: the displacement of the gradient from the tangent space depends on the position of \mathbf{u}_k on the sphere. We illustrate this anisotropy in Fig. 2(b).

(b) Additional radial terms. In the momentum on the sphere \mathbf{c}_k , quantities that are radial (resp. orthogonal) at a point on the sphere may not be radial (resp. orthogonal) at another point. To clarify the contribution of \mathbf{c}_k in the effective learning direction \mathbf{c}_k^\perp , we perform the following decomposition (*cf.* Appendix D.1):

$$\mathbf{c}_k = (\mathbf{c}_k^{\text{grad}} + \lambda r_k^2 \mathbf{c}_k^{L_2}) \otimes \frac{\mathbf{b}_k}{d^{-1/2}\|\mathbf{b}_k\|} \quad \text{with:} \quad (16)$$

$$\mathbf{c}_k^{\text{grad}} \stackrel{\text{def}}{=} \nabla\mathcal{L}(\mathbf{u}_k) + \sum_{i=0}^{k-1} \beta^{k-i} \frac{r_k}{r_i} \nabla\mathcal{L}(\mathbf{u}_i) \quad \text{and} \quad \mathbf{c}_k^{L_2} \stackrel{\text{def}}{=} \mathbf{u}_k + \sum_{i=0}^{k-1} \beta^{k-i} \frac{r_i}{r_k} \mathbf{u}_i. \quad (17)$$

1. Contribution of $\mathbf{c}_k^{\text{grad}}$. At step k , the contribution of each past gradient corresponds to the orthogonal part $\nabla\mathcal{L}(\mathbf{u}_i) - \langle \nabla\mathcal{L}(\mathbf{u}_i), \mathbf{u}_k \rangle \mathbf{u}_k$. It impacts the effective learning direction depending on its orientation relatively to \mathbf{u}_k . Two past points, although equally distant from \mathbf{u}_k on the sphere and with equal gradient amplitude may thus contribute differently in \mathbf{c}_k^\perp due to their orientation (*cf.* Fig. 2(c)).

2. Contribution of $\mathbf{c}_k^{L_2}$. Naturally, the current point \mathbf{u}_k does not contribute to the effective learning direction \mathbf{c}_k^\perp , unlike the history of points in $\sum_{i=0}^{k-1} \beta^{k-i} \frac{r_i}{r_k} \mathbf{u}_i$, which does. This dependency can be avoided if we decouple the L_2 regularization, in which case we do not accumulate L_2 terms in the momentum. This shows that the decoupling proposed in AdamW (Loshchilov & Hutter, 2019) actually removes the contribution of L_2 regularization in the effective learning direction.

(c) The radius ratio $\frac{r_k}{r_i}$ present in both $\mathbf{c}_k^{\text{grad}}$ and $\mathbf{c}_k^{L_2}$ (in inverse proportion) impacts the effective learning direction \mathbf{c}_k^\perp : it can differ for identical sequences $(\mathbf{u}_i)_{i \leq k}$ on the sphere but with distinct radius histories $(r_i)_{i \leq k}$. Since the radius is closely related to the effective learning rate, it means that the effective learning direction \mathbf{c}_k^\perp is adjusted according to the learning rates history.

Note that AdamG (Cho & Lee, 2017), by constraining the optimization to the unit hypersphere and thus removing L_2 regularization, neutralizes all the above phenomena. However, this method has no scheduling effect allowed by the radius dynamics (*cf.* Eq. 14) since it is kept constant during training.

4.2 EMPIRICAL STUDY

To study empirically the importance of the identified geometric phenomena, we perform an ablation study: we compare the performance (accuracy and training loss speed) of Adam and variants that

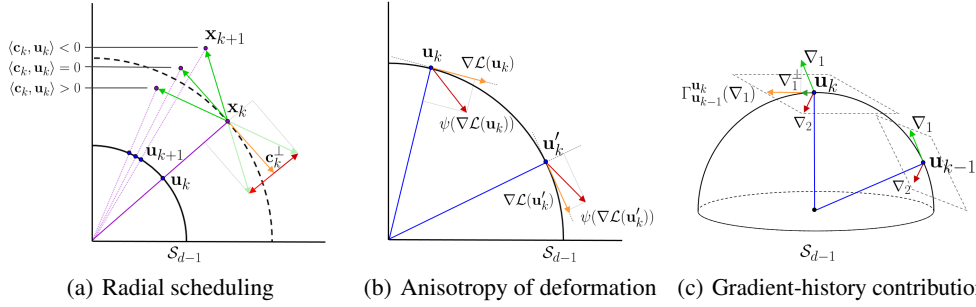


Figure 2: (a) Effect of the radial part of \mathbf{c}_k on the displacement on \mathcal{S}_{d-1} ; (b) Example of anisotropy and sign instability for the deformation $\psi(\nabla \mathcal{L}(\mathbf{u}_k)) = \nabla \mathcal{L}(\mathbf{u}_k) \oslash \frac{|\nabla \mathcal{L}(\mathbf{u}_k)|}{d^{-1/2} \|\nabla \mathcal{L}(\mathbf{u}_k)\|}$ (where $|\cdot|$ is the element-wise absolute value) occurring in Adam’s first optimization step; (c) Different contribution in \mathbf{c}_k^\perp of two past gradients ∇_1 and ∇_2 of equal norm, depending on their orientation. Illustration of the transport of ∇_1 from \mathbf{u}_{k-1} to \mathbf{u}_k : $\Gamma_{\mathbf{u}_{k-1}}^{\mathbf{u}_k}(\nabla_1)$ (cf. Appendix D.2 for details)

neutralize each of them. We recall that AdamW neutralizes **(b2)** and that AdamG neutralizes all of above phenomena but loses the scheduling effect identified in Eq. 14. To complete our analysis, we use geometrical tools to design variations of Adam which neutralizes sequentially each phenomenon while preserving the natural scheduling effect in Theorem 2. We neutralize **(a)** by replacing the element-wise second-order moment, **(b1)** and **(b2)** by transporting the momentum from a current point to the new one, **(c)** by re-scaling the momentum at step k . The details are in Appendix. D.2. The final scheme reads:

$$\mathbf{x}_{k+1} = \mathbf{x}_k - \eta_k \frac{\mathbf{m}_k}{1 - \beta_1^{k+1}} / \sqrt{\frac{v_k}{1 - \beta_2^{k+1}} + \epsilon}, \quad (18)$$

$$\mathbf{m}_k = \beta_1 \frac{r_{k-1}}{r_k} \Gamma_{\mathbf{u}_{k-1}}^{\mathbf{u}_k}(\mathbf{m}_{k-1}) + (1 - \beta_1)(\nabla \mathcal{L}(\mathbf{x}_k) + \lambda \mathbf{x}_k), \quad (19)$$

$$v_k = \beta_2 \frac{r_{k-1}^2}{r_k^2} v_{k-1} + (1 - \beta_2) d^{-1} \|\nabla \mathcal{L}(\mathbf{x}_k) + \lambda \mathbf{x}_k\|^2, \quad (20)$$

where $\Gamma_{\mathbf{u}_{k-1}}^{\mathbf{u}_k}$ is the hypersphere canonical transport from \mathbf{u}_{k-1} to \mathbf{u}_k . Implementation details are in Appendix D.3.

Protocol. For evaluation, we conduct experiments on two architectures: VGG16 (Simonyan & Zisserman, 2015) and ResNet (He et al., 2016) – more precisely ResNet20, a simple variant designed for small images (He et al., 2016), and ResNet18, a popular variant for image classification. We consider three datasets: SVHN (Netzer et al., 2011), CIFAR10 and CIFAR100 (Krizhevsky et al., 2009).

Since our goal is to evaluate the significance of phenomena on radially-invariant parameters, i.e., the convolution filters followed by BN, we only apply variants of Adam including AdamG and AdamW on convolution layers. For comparison consistency, we keep standard Adam on the remaining parameters. We also use a fixed grid hyperparameter search budget and frequency for each method and each architecture (see Appendix D.3 for details).

Results. In Table 2 we report quantitative results of Adam variants across architectures and datasets. In addition, we compare the evolution of the training loss in Fig. 3. We observe that each phenomenon displays a specific trade-off between generalization (accuracy on the test set) and training speed, as following. Neutralizing **(a)** has little effect on the speed over Adam, yet achieves better accuracy. Although it slows down training, neutralizing **(ab)** leads to minima with the overall best accuracy on test set. Note that AdamW[†] neutralizes **(b2)** with its decoupling and is the fastest method, but finds minima with overall worst generalization properties. By constraining the optimization to the hypersphere, AdamG[†] speeds up training over the other variants. Finally, neutralizing **(c)** with Adam w/o **(abc)** brings a slight acceleration, though reaches lower accuracy than Adam w/o **(ab)**. We can see that the revealed geometrical phenomena impact substantially training of BN-equipped CNNs.

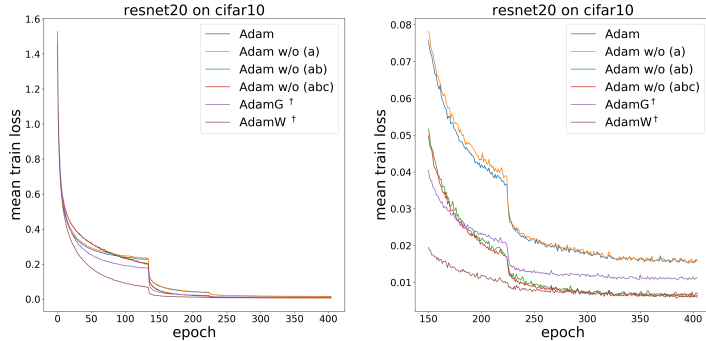


Figure 3: Training speed comparison with ResNet20 on CIFAR10. *Left:* Mean training loss over all training epochs (averaged across 5 seeds) for different Adam variants. *Right:* Zoom-in on the last epochs. Please refer to Table 2 for the corresponding accuracies.

Table 2: Accuracy of Adam and its variants. The figures in this table are the mean top1 accuracy \pm the standard deviation over 5 seeds on the test set for CIFAR10, CIFAR100 and on the validation set for SVHN. † indicates that the original method is only used on convolutional filters while Adam is used for other parameters.

Method	CIFAR10			CIFAR100		SVHN	
	ResNet20	ResNet18	VGG16	ResNet18	VGG16	ResNet18	VGG16
Adam	90.98 \pm 0.06	93.77 \pm 0.20	92.83 \pm 0.17	71.30 \pm 0.36	68.43 \pm 0.16	95.32 \pm 0.23	95.57 \pm 0.20
AdamW†	90.19 \pm 0.24	93.61 \pm 0.12	92.53 \pm 0.25	67.39 \pm 0.27	71.37 \pm 0.22	95.13 \pm 0.15	94.97 \pm 0.08
AdamG†	91.64 \pm 0.17	94.67 \pm 0.12	93.41 \pm 0.17	73.76 \pm 0.34	70.17 \pm 0.20	95.73 \pm 0.05	95.70 \pm 0.25
Adam w/o (a)	91.15 \pm 0.11	93.95 \pm 0.23	92.92 \pm 0.11	74.44 \pm 0.22	68.73 \pm 0.27	95.75 \pm 0.09	95.66 \pm 0.09
Adam w/o (ab)	91.92 \pm 0.18	95.11 \pm 0.10	93.89 \pm 0.09	76.15 \pm 0.25	71.53 \pm 0.19	96.05 \pm 0.12	96.22 \pm 0.09
Adam w/o (abc)	91.81 \pm 0.20	94.92 \pm 0.05	93.75 \pm 0.06	75.28 \pm 0.35	71.45 \pm 0.13	95.84 \pm 0.07	95.82 \pm 0.05

5 RELATED WORK

Understanding Batch Normalization. Albeit conceptually simple, BN has been shown to have complex implications over optimization. The argument of Internal Covariate Shift reduction (Ioffe & Szegedy, 2015) has been challenged and shown to be secondary to smoothing of optimization landscape (Santurkar et al., 2018; Ghorbani et al., 2019) or its modification by creating a different objective function (Lian & Liu, 2019), or enabling of high learning rates through improved conditioning (Bjorck et al., 2018). Arora et al. (2019) demonstrate that (S)GD with BN is robust to the choice of the learning rate, with guaranteed asymptotic convergence, while a similar finding for GD with BN is made by Cai et al. (2019).

Invariances in neural networks. Cho & Lee (2017) propose optimizing over the Grassmann manifold using Riemannian GD. Liu et al. (2017) project weights and activations on the unit hypersphere and compute a function of the angle between them instead of inner products, and subsequently generalize these operators by scaling the angle (Liu et al., 2018). In (Li & Arora, 2020) the radial invariance is leveraged to prove that weight decay (WD) can be replaced by an exponential learning-rate scheduling for SGD with or without momentum. Arora et al. (2019) investigate the radial invariance and show that radius dynamics depends on the past gradients, offering an adaptive behavior to the learning rate. Here we go further and show that SGD projected on the unit hypersphere corresponds to Adam constrained to the hypersphere, and we give an accurate definition of this adaptive behavior.

Effective learning rate. Due to its scale invariance, BN can adaptively adjust the learning rate (van Laarhoven, 2017; Cho & Lee, 2017; Arora et al., 2019; Li & Arora, 2020). van Laarhoven (2017) shows that in BN-equipped networks, WD increases the effective learning rate by reducing the norm of the weights. Conversely, without WD, the norm grows unbounded (Soudry et al., 2018), decreasing the effective learning rate. Zhang et al. (2019) brings additional evidence supporting hypothesis in van Laarhoven (2017), while Hoffer et al. (2018a) finds an exact formulation of the effective learning rate for SGD in normalized networks. In contrast with prior work, we find generic definitions of the effective learning rate with exact expressions for SGD and Adam.

6 CONCLUSION

The spherical framework introduced in this study provides a powerful tool to analyse Adam optimization scheme through its projection on the L_2 unit hypersphere. It allows us to give a precise definition and expression of the effective learning rate for Adam, to relate SGD to a form of Adam, and to identify geometric phenomena which empirically impact training. The framework also brings light to existing variations of Adam, such as L_2 -regularization decoupling. This approach could be extended to other invariances in CNNs such as as filter permutation.

ACKNOWLEDGEMENTS

All experiments in the paper were performed on the valeo.ai gpu cluster infrastructure. We thank Gabriel de Marmiesse for helping us with technical issues.

REFERENCES

- Sanjeev Arora, Zhiyuan Li, and Kaifeng Lyu. Theoretical analysis of auto rate-tuning by batch normalization. In *International Conference on Learning Representations (ICLR)*, 2019.
- Jimmy Lei Ba, Jamie Ryan Kiros, and Geoffrey E Hinton. Layer normalization. *arXiv preprint arXiv:1607.06450*, 2016.
- Nils Bjorck, Carla P Gomes, Bart Selman, and Kilian Q Weinberger. Understanding batch normalization. In *Advances in Neural Information Processing Systems (NeurIPS)*, pp. 7694–7705, 2018.
- Avrim Blum and Ronald L Rivest. Training a 3-node neural network is np-complete. In *Advances in Neural Information Processing Systems (NeurIPS)*, pp. 494–501, 1989.
- Yongqiang Cai, Qianxiao Li, and Zuowei Shen. A quantitative analysis of the effect of batch normalization on gradient descent. In *36th International Conference on Machine Learning (ICML)*, volume 97, 2019.
- Minhyung Cho and Jaehyung Lee. Riemannian approach to batch normalization. In *Advances in Neural Information Processing Systems (NeurIPS)*, pp. 5225–5235, 2017.
- John Duchi, Elad Hazan, and Yoram Singer. Adaptive subgradient methods for online learning and stochastic optimization. *Journal of Machine Learning Research (JMLR)*, 12(Jul):2121–2159, 2011.
- Behrooz Ghorbani, Shankar Krishnan, and Ying Xiao. An investigation into neural net optimization via hessian eigenvalue density. In *36th International Conference on Machine Learning (ICML)*, volume 97, pp. 2232–2241, 2019.
- Kaiming He, Xiangyu Zhang, Shaoqing Ren, and Jian Sun. Deep residual learning for image recognition. In *IEEE Conference on Computer Vision and Pattern Recognition (CVPR)*, pp. 770–778, 2016.
- Elad Hoffer, Ron Banner, Itay Golan, and Daniel Soudry. Norm matters: efficient and accurate normalization schemes in deep networks. In *Advances in Neural Information Processing Systems (NeurIPS)*, pp. 2160–2170, 2018a.
- Elad Hoffer, Itay Hubara, and Daniel Soudry. Fix your classifier: the marginal value of training the last weight layer. *arXiv preprint arXiv:1801.04540*, 2018b.
- Sergey Ioffe and Christian Szegedy. Batch normalization: Accelerating deep network training by reducing internal covariate shift. In *32nd International Conference on Machine Learning (ICML)*, volume 37, pp. 448–456, 2015.
- Diederik P Kingma and Jimmy Ba. Adam: A method for stochastic optimization. In *International Conference on Learning Representations (ICLR)*, 2015.
- Alex Krizhevsky, Geoffrey Hinton, et al. Learning multiple layers of features from tiny images, 2009.

-
- Zhiyuan Li and Sanjeev Arora. An exponential learning rate schedule for deep learning. In *International Conference on Learning Representations (ICLR)*, 2020.
- Xiangru Lian and Ji Liu. Revisit batch normalization: New understanding and refinement via composition optimization. In *The 22nd International Conference on Artificial Intelligence and Statistics (AISTATS)*, pp. 3254–3263, 2019.
- Weiyang Liu, Yan-Ming Zhang, Xingguo Li, Zhiding Yu, Bo Dai, Tuo Zhao, and Le Song. Deep hyperspherical learning. In *Advances in Neural Information Processing Systems (NeurIPS)*, pp. 3950–3960, 2017.
- Weiyang Liu, Zhen Liu, Zhiding Yu, Bo Dai, Rongmei Lin, Yisen Wang, James M Rehg, and Le Song. Decoupled networks. In *IEEE Conference on Computer Vision and Pattern Recognition (CVPR)*, pp. 2771–2779, 2018.
- Ilya Loshchilov and Frank Hutter. Decoupled weight decay regularization. *arXiv preprint arXiv:1711.05101*, 2017.
- Ilya Loshchilov and Frank Hutter. Decoupled weight decay regularization. In *International Conference on Learning Representations (ICLR)*, 2019.
- Yuval Netzer, Tao Wang, Adam Coates, Alessandro Bissacco, Bo Wu, and Andrew Y Ng. Reading digits in natural images with unsupervised feature learning. In *NIPS Workshop on Deep Learning and Unsupervised Feature Learning*, 2011.
- Shibani Santurkar, Dimitris Tsipras, Andrew Ilyas, and Aleksander Madry. How does batch normalization help optimization? In *Advances in Neural Information Processing Systems (NeurIPS)*, pp. 2483–2493, 2018.
- Karen Simonyan and Andrew Zisserman. Very deep convolutional networks for large-scale image recognition. In *International Conference on Learning Representations (ICLR)*, 2015.
- Daniel Soudry, Elad Hoffer, Mor Shpigel Nacson, Suriya Gunasekar, and Nathan Srebro. The implicit bias of gradient descent on separable data. *The Journal of Machine Learning Research (JMLR)*, 19(1):2822–2878, 2018.
- Ilya Sutskever, James Martens, George Dahl, and Geoffrey Hinton. On the importance of initialization and momentum in deep learning. In *30th International Conference on Machine Learning (ICML)*, volume 28, pp. 1139–1147, Atlanta, Georgia, USA, 17–19 Jun 2013.
- Tijmen Tieleman and Geoffrey Hinton. Lecture 6.5-rmsprop: Divide the gradient by a running average of its recent magnitude. *COURSERA: Neural networks for machine learning*, 4(2):26–31, 2012.
- Dmitry Ulyanov, Andrea Vedaldi, and Victor Lempitsky. Instance normalization: The missing ingredient for fast stylization. *arXiv preprint arXiv:1607.08022*, 2016.
- Twan van Laarhoven. L2 regularization versus batch and weight normalization, 2017. *arXiv preprint arXiv:1706.05350*.
- Yuxin Wu and Kaiming He. Group normalization. In *Proceedings of the European Conference on Computer Vision (ECCV)*, pp. 3–19, 2018.
- Guodong Zhang, Chaoqi Wang, Bowen Xu, and Roger Grosse. Three mechanisms of weight decay regularization. In *International Conference on Learning Representations (ICLR)*, 2019.

Supplementary Material to “A spherical analysis of Adam with Batch Normalization”

A RADIAL INVARIANCE OF FILTERS WITH BN

In this section, we show the radial invariance of a set of filters equipped with BN. Please note that the following notations are specific and restricted to this section.

For the sake of simplicity, we only consider the case of a convolutional layer that preserves the spatial extension of the input. We also focus on a single filter. Since all filters act independently on input data, the following calculation holds for any filter.

Let $\mathbf{x} \in \mathbb{R}^{C \times K}$ be the parameters of a single filter, where C is the number of input channels and K is the kernel size. During training, this layer is followed by BN and applied to a batch $\mathbf{s} \in \mathbb{R}^{B \times C \times D}$ of B inputs of spatial size D . The output of the convolution operator ϕ applied to a filter $\mathbf{x} \in \mathbb{R}^{C \times K}$ and to a given batch element $\mathbf{s}_b \in \mathbb{R}^{C \times D}$, with $b \in \llbracket 1, B \rrbracket$, is thus:

$$\mathbf{t}_b \stackrel{\text{def}}{=} \phi(\mathbf{x}, \mathbf{s}_b) \in \mathbb{R}^D. \quad (21)$$

The application $(\mathbf{x}, \mathbf{s}_b) \mapsto \phi(\mathbf{x}, \mathbf{s}_b)$ is bilinear. BN then centers and normalizes the output \mathbf{t} using the mean and variance over the batch and the spatial dimension:

$$\mu = \frac{1}{BD} \sum_{b,j} t_{b,j}, \quad (22)$$

$$\sigma^2 = \frac{1}{BD} \sum_{b,j} (t_{b,j} - \mu)^2, \quad (23)$$

$$\hat{\mathbf{t}}_b \stackrel{\text{def}}{=} (\sigma^2 + \epsilon)^{-1/2} (\mathbf{t}_b - \mu \mathbf{1}_D), \quad (24)$$

where $\mathbf{1}_D$ denotes the all-ones vector of dimension D and ϵ is a small constant.

Now if the coefficients of the filter are rescaled by $\rho > 0$, then, by bilinearity, the new output of the layer for this filter verifies:

$$\tilde{\mathbf{t}}_b = \phi(\rho \mathbf{x}, \mathbf{s}_b) = \rho \phi(\mathbf{x}, \mathbf{s}_b). \quad (25)$$

Since the variance of inputs is generally large in practice, for small ϵ , the mean and variance are:

$$\tilde{\mu} = \rho \mu, \quad (26)$$

$$\tilde{\sigma}^2 \approx \rho^2 \sigma^2. \quad (27)$$

It can then be considered that the subsequent BN layer is invariant to this rescaling, *i.e.*, $\hat{\tilde{\mathbf{t}}}_b \approx \hat{\mathbf{t}}_b$.

B EXTENSION TO OTHER NORMALIZATION LAYERS

The radial invariance for BN described above in Appendix A applies as well to InstanceNorm (IN) (Ulyanov et al., 2016) as the normalization is also done with respect to channels but without the batch dimension. Regarding LayerNorm (Ba et al., 2016) (LN), the normalization is performed over all channels and the entire weight layer can thus be rescaled too, without impacting the output. As for GroupNorm (Wu & He, 2018) (GN), it associates several channels for normalization; the radial invariance in this case concerns the corresponding group of filters.

Thanks to this general property of radial invariance, the results in this paper not only concern BN but also IN. In fact, they apply as well to LN and GN when considering the suitable group of parameters. The optimization in this case concerns the proper slice of the parameter tensor of the layer, *i.e.*, the whole tensor for LN, and the selected group of filters for GN.

C RESULTS IN SECTIONS 2 AND 3

In this section, we provide proofs and/or empirical results supporting the claims in Sections 2 and 3 of the paper.

In the following, the double parentheses around an equation number, e.g., ((10)), indicate that we recall an equation that was previously stated in the main paper, rather than introduce a new one, e.g., noted (28). Also, framed formulas actually refer to results stated in the main paper, thus with double-bracket equation numbering.

C.1 PROOF OF THEOREMS AND VALIDITY OF ASSUMPTIONS

C.1.1 PROOF OF THEOREM 2 (IMAGE STEP ON \mathcal{S}_{d-1} IN SECTION 2.3)

We recall the main theorem in Section 2.3.

Theorem 2 (Image step on \mathcal{S}_{d-1}) *The update of a group of radially-invariant parameters \mathbf{x}_k at step k corresponds to an update of its projection \mathbf{u}_k on \mathcal{S}_{d-1} through an exponential map at \mathbf{u}_k with velocity $\eta_k^e \mathbf{c}_k^\perp$ at order 3:*

$$\mathbf{u}_{k+1} = \text{Exp}_{\mathbf{u}_k} \left(- \left[1 + O \left((\eta_k^e \|\mathbf{c}_k^\perp\|)^2 \right) \right] \eta_k^e \mathbf{c}_k^\perp \right), \quad ((10))$$

where $\text{Exp}_{\mathbf{u}_k}$ is the exponential map on \mathcal{S}_{d-1} , and with

$$\mathbf{c}_k \stackrel{\text{def}}{=} r_k \mathbf{a}_k \oslash \frac{\mathbf{b}_k}{d^{-1/2} \|\mathbf{b}_k\|}, \quad \eta_k^e \stackrel{\text{def}}{=} \frac{\eta_k}{r_k^2 d^{-1/2} \|\mathbf{b}_k\|} \left(1 - \frac{\eta_k \langle \mathbf{c}_k, \mathbf{u}_k \rangle}{r_k^2 d^{-1/2} \|\mathbf{b}_k\|} \right)^{-1}. \quad ((11))$$

More precisely:

$$\mathbf{u}_{k+1} = \frac{\mathbf{u}_k - \eta_k^e \mathbf{c}_k^\perp}{\sqrt{1 + (\eta_k^e \|\mathbf{c}_k^\perp\|)^2}}. \quad ((12))$$

Proof. To simplify the calculation in the demonstration, we introduce the following notation:

$$A_k \stackrel{\text{def}}{=} \frac{\eta_k}{r_k^2 d^{-1/2} \|\mathbf{b}_k\|}. \quad (28)$$

We first demonstrate the expression for the radius dynamics in Eq. (14) and the precise step for \mathbf{u} in Eq. (12). Then we use geometric arguments and a Taylor expansion to derive the update on the sphere stated in Eq.(10).

Radius dynamics. We first show Eq. (14), which we recall here using the A_k notation:

$$\boxed{\frac{r_{k+1}}{r_k} = (1 - A_k \langle \mathbf{c}_k, \mathbf{u}_k \rangle) \sqrt{1 + (\eta_k^e \|\mathbf{c}_k^\perp\|)^2}}. \quad ((14))$$

First, we rewrite the step of a generic scheme in Eqs. (3-4) along the radial and tangential directions and separate the division vector \mathbf{b}_k into its deformation $\frac{\mathbf{b}_k}{d^{-1/2} \|\mathbf{b}_k\|}$ and its scalar scheduling effect $d^{-1/2} \|\mathbf{b}_k\|$, as stated in the discussion:

$$\begin{aligned} r_{k+1} \mathbf{u}_{k+1} &= r_k \mathbf{u}_k - \frac{\eta_k}{d^{-1/2} \|\mathbf{b}_k\|} \mathbf{a}_k \oslash \frac{\mathbf{b}_k}{d^{-1/2} \|\mathbf{b}_k\|} \\ &= r_k \left[\mathbf{u}_k - \frac{\eta_k}{r_k^2 d^{-1/2} \|\mathbf{b}_k\|} r_k \mathbf{a}_k \oslash \frac{\mathbf{b}_k}{d^{-1/2} \|\mathbf{b}_k\|} \right] \\ &= r_k \left[\mathbf{u}_k - A_k r_k \mathbf{a}_k \oslash \frac{\mathbf{b}_k}{d^{-1/2} \|\mathbf{b}_k\|} \right]. \end{aligned} \quad (29)$$

We can note the appearance of a new term $r_k \mathbf{a}_k$. The vector \mathbf{a}_k is a gradient momentum and therefore homogeneous to a gradient. Using Lemma 1, $r_k \mathbf{a}_k$ is homogeneous to a gradient on the hypersphere and can be interpreted as the momentum on the hypersphere.

From Eq. (29), we introduce \mathbf{c}_k (the deformed momentum on hypersphere) as in Eq. (11) and decompose it into the radial and tangential components. We have:

$$\begin{aligned} \frac{r_{k+1}}{r_k} \mathbf{u}_{k+1} &= \mathbf{u}_k - A_k \mathbf{c}_k \\ &= (1 - A_k \langle \mathbf{c}_k, \mathbf{u}_k \rangle) \mathbf{u}_k - A_k \mathbf{c}_k^\perp. \end{aligned} \quad (30)$$

By taking the squared norm of the equation, we obtain:

$$\frac{r_{k+1}^2}{r_k^2} = (1 - A_k \langle \mathbf{c}_k, \mathbf{u}_k \rangle)^2 + (A_k \|\mathbf{c}_k^\perp\|)^2. \quad (31)$$

Making the assumption that $1 - A_k \langle \mathbf{c}_k, \mathbf{u}_k \rangle > 0$, which is true in practice and discussed in the next subsection, we have:

$$\frac{r_{k+1}}{r_k} = (1 - A_k \langle \mathbf{c}_k, \mathbf{u}_k \rangle) \sqrt{1 + \left(\frac{A_k}{1 - A_k \langle \mathbf{c}_k, \mathbf{u}_k \rangle} \|\mathbf{c}_k^\perp\| \right)^2}. \quad (32)$$

After introducing $\eta_k^e = \frac{A_k}{(1 - A_k \langle \mathbf{c}_k, \mathbf{u}_k \rangle)}$ as in Eq. (11), we obtain the result of (14).

Update of normalized parameters. We then show Eq. (12):

$$\boxed{\mathbf{u}_{k+1} = \frac{\mathbf{u}_k - \eta_k^e \mathbf{c}_k^\perp}{\sqrt{1 + (\eta_k^e \|\mathbf{c}_k^\perp\|)^2}}}. \quad (12)$$

Combining the radius dynamics previously calculated with Eq. (30), we have:

$$\mathbf{u}_{k+1} = \frac{(1 - A_k \langle \mathbf{c}_k, \mathbf{u}_k \rangle) \mathbf{u}_k - A_k \mathbf{c}_k^\perp}{(1 - A_k \langle \mathbf{c}_k, \mathbf{u}_k \rangle) \sqrt{1 + (\eta_k^e \|\mathbf{c}_k^\perp\|)^2}} \quad (33)$$

$$= \frac{\mathbf{u}_k - \frac{A_k}{1 - A_k \langle \mathbf{c}_k, \mathbf{u}_k \rangle} \mathbf{c}_k^\perp}{\sqrt{1 + (\eta_k^e \|\mathbf{c}_k^\perp\|)^2}}. \quad (34)$$

Hence the result (12) using the definition of η_k^e .

This result provides a unique decomposition of the generic step as a step in $\text{span}(\mathbf{u}_k, \mathbf{c}_k^\perp)$ for the normalized filter (Eq. (12)) and as a radius update (Eq. (14)).

We split the rest of the proof of the theorem in three parts.

Distance covered on the sphere. The distance covered on the hypersphere \mathcal{S}_{d-1} by an optimization step is:

$$\text{dist}_{\mathcal{S}_{d-1}}(\mathbf{u}_{k+1}, \mathbf{u}_k) = \arccos(\langle \mathbf{u}_{k+1}, \mathbf{u}_k \rangle). \quad (35)$$

From Eq. (12) and with Lemma 1, we also have:

$$\langle \mathbf{u}_{k+1}, \mathbf{u}_k \rangle = \frac{1}{\sqrt{1 + (\eta_k^e \|\mathbf{c}_k^\perp\|)^2}}. \quad (36)$$

Therefore, $\text{dist}_{\mathcal{S}_{d-1}}(\mathbf{u}_{k+1}, \mathbf{u}_k) = \varphi(\eta_k^e \|\mathbf{c}_k^\perp\|)$ where $\varphi : z \mapsto \arccos\left(\frac{1}{\sqrt{1+z^2}}\right)$, which is equal to arctan on \mathbb{R}_+ . Then a Taylor expansion at order 3 of arctan yields for $\eta_k^e \|\mathbf{c}_k^\perp\|$:

$$\text{dist}_{\mathcal{S}_{d-1}}(\mathbf{u}_{k+1}, \mathbf{u}_k) = \eta_k^e \|\mathbf{c}_k^\perp\| + O\left((\eta_k^e \|\mathbf{c}_k^\perp\|)^3\right). \quad (37)$$

The Taylor expansion validity is discussed in the next subsection.

Exponential map on the sphere. Given a Riemannian manifold \mathcal{M} , for a point $\mathbf{u} \in \mathcal{M}$ there exists an open set \mathcal{O} of the tangent space $\mathcal{T}_{\mathbf{u}}\mathcal{M}$ containing $\mathbf{0}$, such that for any tangent vector $\mathbf{w} \in \mathcal{O}$ there is a unique geodesic (a path minimizing the local distance on \mathcal{M} when conserving the tangent velocity) $\gamma : [-1, 1] \rightarrow \mathcal{M}$ that is differentiable and such that $\gamma(0) = \mathbf{u}$ and $\gamma'(0) = \mathbf{w}$. Then, the exponential map of \mathbf{w} from \mathbf{u} is defined as $\text{Exp}_{\mathbf{u}}(\mathbf{w}) = \gamma(1)$.

In the case of the manifold \mathcal{S}_{d-1} , the geodesics are complete (they are well defined for any point $\mathbf{u} \in \mathcal{S}_{d-1}$ and any velocity $\mathbf{w} \in \mathcal{T}_{\mathbf{u}}\mathcal{S}_{d-1}$) and are the great circles: for any $\mathbf{u} \in \mathcal{S}_{d-1}$ and any $\mathbf{w} \in \mathcal{T}_{\mathbf{u}}\mathcal{S}_{d-1}$, the map $\psi : t \in \mathbb{R} \mapsto \text{Exp}_{\mathbf{u}}(t\mathbf{w})$ verifies $\psi(\mathbb{R}) = \mathcal{S}_{d-1} \cap \text{span}(\{\mathbf{u}, \mathbf{w}\})$ which is a great circle passing through \mathbf{u} with tangent \mathbf{w} . Furthermore, since the circumference of the great circle is 2π , we have that for any $\mathbf{p} \in \mathcal{S}_{d-1} \setminus \{-\mathbf{u}\}$ there is a unique \mathbf{w} verifying $\|\mathbf{w}\| < \pi$ such that $\mathbf{p} = \text{Exp}_{\mathbf{u}}(\mathbf{w})$ and we have:

$$\text{dist}_{\mathcal{S}_{d-1}}(\mathbf{u}, \mathbf{p}) = \|\mathbf{w}\| \text{ and } \langle \mathbf{p}, \mathbf{w} \rangle \geq 0. \quad (38)$$

Optimization step as an exponential map. We will use the previously stated differential geometry properties to prove:

$$\mathbf{u}_{k+1} = \text{Exp}_{\mathbf{u}_k} \left(- \left[1 + O \left((\eta_k^e \|\mathbf{c}_k^\perp\|)^2 \right) \right] \eta_k^e \mathbf{c}_k^\perp \right). \quad (10)$$

For an optimization step we have:

- by construction, $\mathbf{c}_k^\perp \in \mathcal{T}_{\mathbf{u}_k}\mathcal{S}_{d-1}$;
- from Eq. (12), $\mathbf{u}_{k+1} \in \mathcal{S}_{d-1} \cap \text{span}(\{\mathbf{u}_k, \mathbf{c}_k^\perp\})$;
- from Eq. (12), $\langle \mathbf{u}_{k+1}, \mathbf{c}_k^\perp \rangle \leq 0$.

Then, there exists α that verifies $\|\alpha \mathbf{c}_k^\perp\| < \pi$ such that:

$$\mathbf{u}_{k+1} = \text{Exp}_{\mathbf{u}_k} (\alpha \mathbf{c}_k^\perp). \quad (39)$$

From Eq. (38), because $\langle \mathbf{u}_{k+1}, \mathbf{c}_k^\perp \rangle \leq 0$, we have $\alpha < 0$. We also have that $\|\alpha \mathbf{c}_k^\perp\| = \text{dist}_{\mathcal{S}_{d-1}}(\mathbf{u}_{k+1}, \mathbf{u}_k)$. Then, using the distance previously calculated in Eq. (37), we have:

$$|\alpha| \|\mathbf{c}_k^\perp\| = \eta_k^e \|\mathbf{c}_k^\perp\| + O \left((\eta_k^e \|\mathbf{c}_k^\perp\|)^3 \right), \quad (40)$$

$$|\alpha| = \eta_k^e \left[1 + O \left((\eta_k^e \|\mathbf{c}_k^\perp\|)^2 \right) \right]. \quad (41)$$

Combining the sign and absolute value of α , we get the final exponential map expression:

$$\mathbf{u}_{k+1} = \text{Exp}_{\mathbf{u}_k} \left(- \left[1 + O \left((\eta_k^e \|\mathbf{c}_k^\perp\|)^2 \right) \right] \eta_k^e \mathbf{c}_k^\perp \right), \quad (10)$$

$$\approx \text{Exp}_{\mathbf{u}_k} (-\eta_k^e \mathbf{c}_k^\perp). \quad (42)$$

Note that we implicitly assume here that $|\alpha| \|\mathbf{c}_k^\perp\| \approx \eta_k^e \|\mathbf{c}_k^\perp\| < \pi$, which is discussed in the next subsection. □

C.1.2 VALIDITY OF THE ASSUMPTIONS IN THEOREM 2

Sign of $1 - A_k \langle \mathbf{c}_k, \mathbf{u}_k \rangle$. We tracked the maximum of the quantity $A_k \langle \mathbf{c}_k, \mathbf{u}_k \rangle$ for all the filters of a ResNet20 CIFAR trained on CIFAR10 and optimized with SGD-M or Adam (see Appendix D.3 for implementation details). As can be seen on Fig. 4, this quantity is always small compared to 1, making $1 - A_k \langle \mathbf{c}_k, \mathbf{u}_k \rangle$ always positive in practice. The order of magnitude of this quantity is roughly the same for different architectures and datasets.

Taylor expansion. We tracked the maximum of the quantity $\eta_k^e \|\mathbf{c}_k^\perp\|$ for all the filters of a ResNet20 CIFAR trained on CIFAR10 and optimized with SGD-M or Adam. The observed values justify the Taylor expansion and validate the assumption $|\alpha| \|\mathbf{c}_k^\perp\| \approx \eta_k^e \|\mathbf{c}_k^\perp\| < \pi$. (cf. Fig 5). The order of magnitude of this quantity is roughly the same for other different architectures and datasets.

C.1.3 ν_k ORDER 2 MOMENT ON THE HYPERSPHERE FOR ADAM

Scheduling effect of Adam division vector. With Eq. (64) and using Lemma 1, we can give the expression of the second-order moment on the sphere, defined as $\nu_k = r_k d^{-1/2} \|\mathbf{b}_k\|$:

$$\nu_k = d^{-1/2} \frac{1 - \beta_1^{k+1}}{1 - \beta_1} \left(\frac{1 - \beta_2}{1 - \beta_2^{k+1}} \right)^{1/2} \left(\sum_{i=0}^k \beta_2^{k-i} \frac{r_k^2}{r_i^2} \|\nabla \mathcal{L}(\mathbf{u}_i) + \lambda r_i^2 \mathbf{u}_i\|^2 \right)^{1/2}. \quad (43)$$

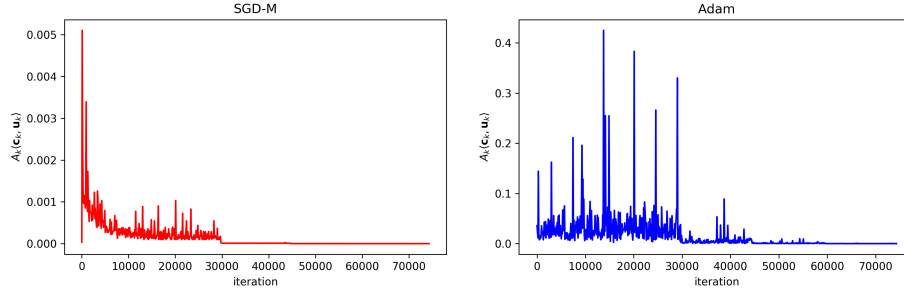


Figure 4: **Tracking of $A_k\langle \mathbf{c}_k, \mathbf{u}_k \rangle$ for SGD-M and Adam.** The above graphs show the maximum of the absolute value of $A_k\langle \mathbf{c}_k, \mathbf{u}_k \rangle$ for all filters in all layers of a ResNet20 CIFAR trained on CIFAR10 and optimized with SGD-M (left) or Adam (right). The quantity is always small compared to 1. Therefore we may assume that $1 - A_k\langle \mathbf{c}_k, \mathbf{u}_k \rangle \geq 0$.

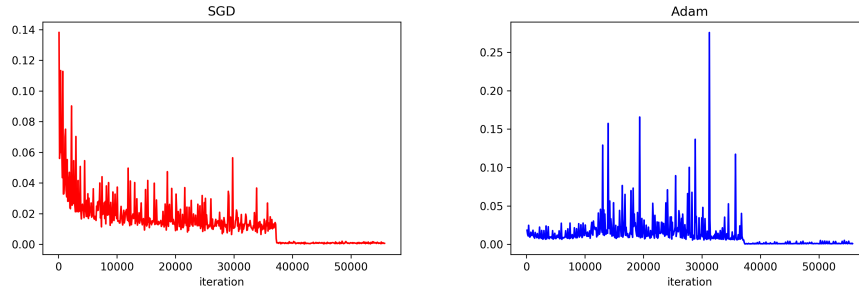


Figure 5: **Tracking of $\eta_k^e \|\mathbf{c}_k^\perp\|$ for SGD-M and Adam.** The above graphs show the maximum of the absolute value of $\eta_k^e \|\mathbf{c}_k^\perp\|$ for all filters in all layers of a ResNet20 CIFAR trained on CIFAR10 and optimized with SGD-M (left) or Adam (right).

C.1.4 PROOF OF THEOREM 4 (SGD EQUIVALENT SCHEME ON THE UNIT HYPERSPHERE) IN SECTION 3.2

We prove the following theorem:

Theorem 4 (SGD equivalent scheme on the unit hypersphere.) *For any $\lambda > 0, \eta > 0, r_0 > 0$, we have the following equivalence at order 2 in the radius dynamics:*

$$\left\{ \begin{array}{l} \text{(SGD)} \\ \mathbf{x}_0 = r_0 \mathbf{u}_0 \\ \lambda_k = \lambda \\ \eta_k = \eta \end{array} \right. \text{ is scheme-equivalent at order 2 to } \left\{ \begin{array}{l} \text{(AdamG}^*) \\ \mathbf{x}_0 = \mathbf{u}_0 \\ \beta = (1 - \eta\lambda)^4 \\ \eta_k = (2\beta)^{-1/2} \\ v_0 = r_0^4 (2\eta^2 \beta^{1/2})^{-1} \end{array} \right.$$

Proof. As summarized in Table 1, the expressions of the effective learning rates and directions for SGD are $\mathbf{c}_k^\perp = r_k \nabla \mathcal{L}(\mathbf{x}_k) = \nabla \mathcal{L}(\mathbf{u}_k)$ and $\eta_k^e = \frac{\eta_k}{r_k^2(1-\eta_k\lambda_k)}$.

Equivalence with SGD and L_2 regularization. We look for conditions leading to an equivalence between SGD with L_2 regularization and SGD without L_2 regularization. Using Lemma 3, the equality of effective directions is trivial and the equality of effective learning rates for any step k yields the following equivalence:

$$\left\{ \begin{array}{l} \text{(SGD)} \\ \tilde{\mathbf{x}}_0 = r_0 \mathbf{u}_0 \\ \tilde{\lambda}_k = \lambda \\ \tilde{\eta}_k = \eta \end{array} \right. \text{ is scheme-equivalent to } \left\{ \begin{array}{l} \text{(SGD)} \\ \mathbf{x}_0 = r_0 \mathbf{u}_0 \\ \lambda_k = 0 \\ \eta_k = \eta(1 - \eta\lambda)^{-2k-1} \end{array} \right. \quad (44)$$

L_2 regularization is equivalent to an exponential scheduling of the learning rate, as found in Li & Arora (2020). Here, we provide a proof in a constructive manner. We are going to use Lemma 3 and

find a sufficient condition to have:

$$\begin{cases} \text{(i)} \mathbf{u}_0 = \tilde{\mathbf{u}}_0 \\ \text{(ii)} \forall k \geq 0, \eta_k^e = \tilde{\eta}_k^e, \mathbf{c}_k^\perp = \tilde{\mathbf{c}}_k^\perp. \end{cases}$$

Equation (i) is trivially satisfied by simply taking the same starting point: $\tilde{\mathbf{x}}_0 = \mathbf{x}_0$.

Regarding (ii), because effective directions are the same and only depend on \mathbf{u}_k , we only need a sufficient condition on η_k^e . For effective learning rates, using Eq. ((14)) and expressions in Table 1, we have:

$$\eta_k^e = \tilde{\eta}_k^e \Leftrightarrow \frac{\eta_k}{r_k^2} = \frac{\tilde{\eta}_k}{\tilde{r}_k^2(1 - \tilde{\eta}_k\lambda)}. \quad (45)$$

Since $\tilde{\eta}_k = \eta$, we obtain:

$$(45) \Leftrightarrow \eta_k = \left(\frac{r_k}{\tilde{r}_k}\right)^2 \frac{\eta}{(1 - \eta\lambda)}.$$

Therefore:

$$\frac{\eta_{k+1}}{\eta_k} = \left(\frac{r_{k+1}\tilde{r}_k}{\tilde{r}_{k+1}r_k}\right)^2 = \left(\frac{r_{k+1}/r_k}{\tilde{r}_{k+1}/\tilde{r}_k}\right)^2.$$

By using the radius dynamics in Eq. (14) for the two schemes, SGD and SGD with L_2 regularization, and by the equality of effective learning rates and directions, we have:

$$\begin{aligned} \frac{\eta_{k+1}}{\eta_k} &= \left(\frac{\sqrt{1 + (\eta_k^e \|\mathbf{c}_k^\perp\|)^2}}{(1 - \eta\lambda)\sqrt{1 + (\tilde{\eta}_k^e \|\tilde{\mathbf{c}}_k^\perp\|)^2}}\right)^2 \\ &= (1 - \eta\lambda)^{-2}. \end{aligned}$$

By taking Eq. (45) for $k = 0$, because $r_0 = \tilde{r}_0$ we have: $\eta_0 = \eta(1 - \eta\lambda)^{-1}$. Combining the previous relation and the initialization case, we derive by induction that $\eta_k = \eta(1 - \eta\lambda)^{-2k-1}$ is a sufficient condition. We can conclude, using Lemma 3, the equivalence stated in Eq. (44).

Resolution of the radius dynamics. Without L_2 regularization, the absence of radial component in \mathbf{c}_k makes the radius dynamics simple:

$$r_{k+1}^2 = r_k^2 + \frac{(\eta_k \|\nabla \mathcal{L}(\mathbf{u}_k)\|)^2}{r_k^2}. \quad (46)$$

With a Taylor expansion at order 2, we can show that for $k \geq 1$ the solution $r_k^2 = \sqrt{2 \sum_{i=0}^{k-1} (\eta_i \|\nabla \mathcal{L}(\mathbf{u}_i)\|)^2 + r_0^4}$ satisfies the previous equation. Indeed using the expression at step $k + 1$ gives:

$$\begin{aligned} r_{k+1}^2 &= \sqrt{2 \sum_{i=0}^{k-1} (\eta_i \|\nabla \mathcal{L}(\mathbf{u}_i)\|)^2 + r_0^4 + 2(\eta_k \|\nabla \mathcal{L}(\mathbf{u}_k)\|)^2} \\ &= r_k^2 \sqrt{1 + 2 \frac{(\eta_k \|\nabla \mathcal{L}(\mathbf{u}_k)\|)^2}{r_k^4}} \\ &= r_k^2 \left(1 + (1/2)2 \frac{(\eta_k \|\nabla \mathcal{L}(\mathbf{u}_k)\|)^2}{r_k^4} + o\left(\frac{(\eta_k \|\nabla \mathcal{L}(\mathbf{u}_k)\|)^2}{r_k^4}\right)\right) \\ &= r_k^2 + \frac{(\eta_k \|\nabla \mathcal{L}(\mathbf{u}_k)\|)^2}{r_k^2} + o\left(\frac{(\eta_k \|\nabla \mathcal{L}(\mathbf{u}_k)\|)^2}{r_k^2}\right). \end{aligned}$$

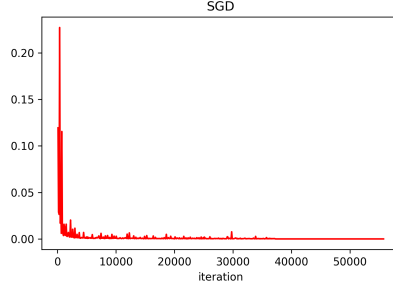


Figure 6: **Validity of Taylor expansion.** We tracked the maximum value of $(\eta_k \|\nabla \mathcal{L}(\mathbf{u}_k)\|)^2 / r_k^2$ for all filters in all layers of a ResNet20 CIFAR trained on CIFAR10 with SGD. The order of magnitude of the gradient is roughly the same for other architectures or datasets. It empirically validates the approximation by the Taylor expansion.

Using $\eta_k = \eta(1 - \eta\lambda)^{-2k-1}$, introducing $\beta = (1 - \eta\lambda)^4$, omitting the $o\left(\frac{(\eta_k \|\nabla \mathcal{L}(\mathbf{u}_k)\|)^2}{r_k^2}\right)$ and injecting the previous solution in the effective learning rate, we obtain the closed form:

$$\begin{aligned} \eta_k^e &= \frac{\eta(1 - \eta\lambda)^{-2k-1}}{\sqrt{2 \sum_{i=0}^{k-1} \eta^2 (1 - \eta\lambda)^{-4i-2} \|\nabla \mathcal{L}(\mathbf{u}_i)\|^2 + r_0^4}} \\ &= \frac{(2\beta)^{-\frac{1}{2}}}{\sqrt{\sum_{i=0}^{k-1} \beta^{(k-1)-i} \|\nabla \mathcal{L}(\mathbf{u}_i)\|^2 + \beta^k \frac{r_0^4}{2\eta^2 \beta^{\frac{1}{2}}}}}. \end{aligned} \quad (47)$$

AdamG*. The AdamG* scheme is constrained on the hypersphere thanks to the normalization; the radius is therefore constant and equal to 1. The absence of radial component in the update gives: $\mathbf{c}_k^\perp = \nabla \mathcal{L}(\mathbf{u}_k)$ and $\eta_k^e = \frac{\eta_k}{\sqrt{v_k}}$. Thus, the resolution of the induction on v_k leads to the closed form:

$$\eta_k^e = \frac{\eta_k}{\sqrt{\sum_{i=0}^{k-1} \beta^{(k-1)-i} \|\nabla \mathcal{L}(\mathbf{u}_i)\|^2 + \beta^k v_0}}. \quad (48)$$

Hence the final theorem, when identifying the closed-form expressions of effective learning rates and using Lemma 3. \square

C.1.5 VALIDITY OF THE ASSUMPTIONS IN THEOREM 4

Validity of the Taylor expansion. We tracked, for a CNN trained with SGD, the quantity $(\eta_k \|\nabla \mathcal{L}(\mathbf{u}_k)\|)^2 / r_k^2$, which is the variable of the Taylor expansion. As can be seen in Figure 6, the typical order of magnitude is 10^{-2} , justifying the Taylor expansion.

A quick formal analysis also suggests the validity of this hypothesis. Thanks to the expression of $\eta_k = (1 - \eta\lambda)^{-2i-k} \eta$ shown in the previous section, if we replace $\|\nabla \mathcal{L}(\mathbf{u}_k)\|$ by a constant for asymptotic analysis, the comparison becomes:

$$(1 - \eta\lambda)^{-4k-2} \ll (1 - \eta\lambda)^{-2} \frac{1 - (1 - \eta\lambda)^{-4k}}{1 - (1 - \eta\lambda)^{-4}} \quad (49)$$

$$1 \ll \frac{1 - (1 - \eta\lambda)^{4k}}{(1 - \eta\lambda)^{-4} - 1}. \quad (50)$$

It is asymptotically true.

D RESULTS IN SECTION 4 (GEOMETRIC PHENOMENA IN ADAM OPTIMIZATION)

D.1 RESULTS IN SECTION 4.2 (IDENTIFICATION OF GEOMETRICAL PHENOMENA IN ADAM)

Decomposition of the effective direction. We decompose the effective direction as a gradient term and an L_2 regularization term:

$$\mathbf{c}_k^{\text{grad}} = \nabla \mathcal{L}(\mathbf{u}_k) + \sum_{i=0}^{k-1} \beta^{k-i} \frac{r_k}{r_i} \nabla \mathcal{L}(\mathbf{u}_i), \quad ((17))$$

$$\mathbf{c}_k^{L_2} = \mathbf{u}_k + \sum_{i=0}^{k-1} \beta^{k-i} \frac{r_i}{r_k} \mathbf{u}_i. \quad ((17))$$

Note that these expressions highlight the main terms at step k and the dependency on r_i .

Developing the recurrence in Eq (4), we obtain:

$$\mathbf{a}_k = \sum_{i=0}^k \beta^{k-i} (\nabla \mathcal{L}(\mathbf{x}_i) + \lambda \mathbf{x}_i). \quad (51)$$

Using Lemma 1 and decomposing on $\nabla \mathcal{L}(\mathbf{u}_i)$ and \mathbf{u}_i , we have:

$$\mathbf{a}_k = \sum_{i=0}^k \beta^{k-i} \left(\frac{1}{r_i} \nabla \mathcal{L}(\mathbf{u}_i) + \lambda r_i \mathbf{u}_i \right) \quad (52)$$

$$= \frac{1}{r_k} \left(\sum_{i=0}^k \beta^{k-i} \left(\frac{r_k}{r_i} \nabla \mathcal{L}(\mathbf{u}_i) + \lambda r_k r_i \mathbf{u}_i \right) \right). \quad (53)$$

Thus:

$$r_k \mathbf{a}_k = \sum_{i=0}^k \beta^{k-i} \frac{r_k}{r_i} \nabla \mathcal{L}(\mathbf{u}_i) + \lambda r_k^2 \sum_{i=0}^k \beta^{k-i} \frac{r_i}{r_k} \mathbf{u}_i, \quad (54)$$

which leads to the expression of $\mathbf{c}_k^{\text{grad}}$ and $\mathbf{c}_k^{L_2}$ when we define $\mathbf{c}_k \stackrel{\text{def}}{=} r_k \mathbf{a}_k \oslash \frac{\mathbf{b}_k}{d^{-1/2} \|\mathbf{b}_k\|}$ (Eq. (11)).

D.2 RESULTS IN SECTION 4.2 (EMPIRICAL STUDY)

Clarification on Adam without deformation of gradients (a). Following Theorem 2, the division vector \mathbf{b}_k has two contributions in the decomposition:

- a deformation in \mathbf{c}_k applied to \mathbf{a}_k : $\mathbf{c}_k = r_k \mathbf{a}_k \oslash \frac{\mathbf{b}_k}{d^{-1/2} \|\mathbf{b}_k\|}$;
- a scheduling effect in the effective learning rate $d^{-1/2} \|\mathbf{b}_k\|$ (Eq. (11)).

The goal is to find a new division vector $\mathbf{S}(\mathbf{b}_k)$ that does not create a deformation while preserving the scheduling effect of \mathbf{b}_k in the effective learning rate. This means:

$$\frac{\mathbf{S}(\mathbf{b}_k)}{d^{-1/2} \|\mathbf{S}(\mathbf{b}_k)\|} = [1 \cdots 1]^\top, \quad (55)$$

$$d^{-1/2} \|\mathbf{S}(\mathbf{b}_k)\| = d^{-1/2} \|\mathbf{b}_k\|. \quad (56)$$

This leads to $\mathbf{S}(\mathbf{b}_k) = d^{-1/2} \|\mathbf{b}_k\| [1 \cdots 1]^\top$.

In the case of $\beta_1 = 0$, $\mathbf{a}_k = \nabla \mathcal{L}(\mathbf{x}_k)$, for any \mathbf{b}_k . When we apply the standardization, we obtain:

$$\mathbf{c}_k = r_k \nabla \mathcal{L}(\mathbf{x}_k) \oslash \frac{\mathbf{S}(\mathbf{b}_k)}{d^{-1/2} \|\mathbf{S}(\mathbf{b}_k)\|} = \nabla \mathcal{L}(\mathbf{u}_k) \oslash [1 \cdots 1]^\top = \nabla \mathcal{L}(\mathbf{u}_k). \quad (57)$$

The direction lies in the tangent space because, by Lemma 1, the gradient belongs to it.

In the generic scheme, using the standardization gives:

$$\mathbf{x}_{k+1} = \mathbf{x}_k - \eta_k \mathbf{a}_k \odot \mathcal{S}(\mathbf{b}_k) \quad (58)$$

$$= \mathbf{x}_k - \eta_k \mathbf{a}_k \odot (d^{-1/2} \|\mathbf{b}_k\| [1 \cdots 1]^\top) \quad (59)$$

$$= \mathbf{x}_k - \eta_k \mathbf{a}_k / (d^{-1/2} \|\mathbf{b}_k\|). \quad (60)$$

This means that the standardization consists in replacing the Hadamard division by \mathbf{b}_k with a scalar division by $d^{-1/2} \|\mathbf{b}_k\|$.

In the case of Adam, we recall that:

$$\mathbf{b}_k = \frac{1 - \beta_1^{k+1}}{1 - \beta_1} \sqrt{\frac{\mathbf{v}_k}{1 - \beta_2^{k+1}}} + \epsilon. \quad (9)$$

Omitting ϵ for simplicity we have:

$$d^{-1/2} \|\mathbf{b}_k\| = \frac{1 - \beta_1^{k+1}}{1 - \beta_1} \left(\frac{1}{1 - \beta_2^{k+1}} \right)^{\frac{1}{2}} d^{-1/2} \|\sqrt{\mathbf{v}_k}\|. \quad (61)$$

Let us calculate $\|\sqrt{\mathbf{v}_k}\|$. Developing the recursion of \mathbf{v}_k , as defined in Eq. (8), leads to:

$$\mathbf{v}_k = (1 - \beta_2) \sum_{i=0}^k \beta_2^{k-i} (\nabla \mathcal{L}(\mathbf{x}_i) + \lambda \mathbf{x}_i)^2, \quad (62)$$

$$\sqrt{\mathbf{v}_k} = \sqrt{1 - \beta_2} \sqrt{\sum_{i=0}^k \beta_2^{k-i} (\nabla \mathcal{L}(\mathbf{x}_i) + \lambda \mathbf{x}_i)^2}, \quad (63)$$

where the square and the square-root are element-wise operations. Hence, if we take the square norm:

$$\begin{aligned} \|\sqrt{\mathbf{v}_k}\|^2 &= (1 - \beta_2) \sum_{j=1}^d \left(\sqrt{\sum_{i=0}^k \beta_2^{k-i} (\nabla \mathcal{L}(\mathbf{x}_i) + \lambda \mathbf{x}_i)^2} \right)_j^2 \\ &= (1 - \beta_2) \sum_{j=1}^d \sum_{i=0}^k \beta_2^{k-i} (\nabla \mathcal{L}(\mathbf{x}_i) + \lambda \mathbf{x}_i)_j^2 \\ &= (1 - \beta_2) \sum_{i=0}^k \beta_2^{k-i} \sum_{j=1}^d (\nabla \mathcal{L}(\mathbf{x}_i) + \lambda \mathbf{x}_i)_j^2 \\ &= (1 - \beta_2) \sum_{i=0}^k \beta_2^{k-i} \|\nabla \mathcal{L}(\mathbf{x}_i) + \lambda \mathbf{x}_i\|^2, \end{aligned} \quad (64)$$

where the j subscript denotes the j -th element of the vector. It is exactly the order-2 moment of the gradient norm.

Therefore, we define the scalar v_k :

$$v_k = \beta_2 v_{k-1} + (1 - \beta_2) d^{-1} \|\nabla \mathcal{L}(\mathbf{x}_k) + \lambda \mathbf{x}_k\|^2, \quad (65)$$

which is the order-2 moment of the gradient norm with a factor d^{-1} . It verifies $\sqrt{v_k} = d^{-1/2} \|\sqrt{\mathbf{v}_k}\|$, needed for the scalar division stated in Eq. (61). By applying the bias correction, it gives the formula given in the paper of Adam w/o (a):

$$\mathbf{x}_{k+1} = \mathbf{x}_k - \eta_k \frac{\mathbf{m}_k}{1 - \beta_1^{k+1}} / \sqrt{\frac{v_k}{1 - \beta_2^{k+1}}} + \epsilon, \quad (66)$$

$$\mathbf{m}_k = \beta_1 \mathbf{m}_{k-1} + (1 - \beta_1) (\nabla \mathcal{L}(\mathbf{x}_k) + \lambda \mathbf{x}_k), \quad (67)$$

$$v_k = \beta_2 v_{k-1} + (1 - \beta_2) d^{-1} \|\nabla \mathcal{L}(\mathbf{x}_k) + \lambda \mathbf{x}_k\|^2. \quad (68)$$

Note that the previous demonstration makes the factor d^{-1} appear in v_k to have exactly the scheduling effect of Adam without the deformation.

Clarification on Adam without deformed gradients and no additional radial terms (ab).

We introduce the rescaling and transport transformation of the momentum to neutralize the identified effects on the effective direction (cf. Section 4.2). The resulting, new \mathbf{c}_k is orthogonal to \mathbf{u}_k and does not contribute in the effective learning rate tuning with its radial part.

To avoid gradient history leaving the tangent space and thus neutralize **(b)**, we perform a parallel transport of the momentum \mathbf{a}_{k-1} from the corresponding point on the sphere \mathbf{u}_{k-1} to the new point \mathbf{u}_k denoted as $\Gamma_{\mathbf{u}_{k-1}}^{\mathbf{u}_k}(\mathbf{a}_{k-1})$ at each iteration $k \geq 1$. Figure 2(c) illustrates the transport of a gradient. The parallel transport between two points associates each vector of the tangent space of the first point to a vector of the second tangent space by preserving the scalar product with the derivatives along the geodesic. Consequently, the gradients accumulated in the resulting momentum now lie in the tangent space of \mathbf{u}_k at each step. This neutralizes the additional radial terms phenomena from $\mathbf{c}_k^{\text{grad}}$. Since \mathbf{u}_{k-1} , \mathbf{u}_k and \mathbf{a}_k are coplanar, the transport of the momentum on the hypersphere can be expressed as a rotation:

$$\mathbb{T}(\mathbf{a}_{k-1}) \stackrel{\text{def}}{=} \Gamma_{\mathbf{u}_{k-1}}^{\mathbf{u}_k}(\mathbf{a}_{k-1}) = \langle \mathbf{u}_{k-1}, \mathbf{u}_k \rangle \mathbf{a}_{k-1} - \langle \mathbf{a}_{k-1}, \mathbf{u}_k \rangle \mathbf{u}_{k-1}, \quad (69)$$

$$\mathbf{a}_k = \beta \mathbb{T}(\mathbf{a}_{k-1}) + \nabla \mathcal{L}(\mathbf{x}_k) + \lambda \mathbf{x}_k. \quad (70)$$

Although the transport operation is strictly defined on the tangent space only, the scalar product formulation enables its extension to the whole space. The transformation is linear and $\mathbb{T}(\mathbf{u}_{k-1}) = 0$. We thus have:

$$\mathbb{T}(\mathbf{a}_{k-1} - \lambda \mathbf{u}_{k-1}) = \mathbb{T}(\mathbf{a}_{k-1}). \quad (71)$$

In the previous formulation, we see that the L_2 component is not transported and does not contribute in the new momentum. Finally, the momentum only contains the contribution of the current L_2 regularization. This means that the RT transformation decouples the L_2 regularization and thus neutralizes the additional radial terms from $\mathbf{c}_k^{L_2}$.

Clarification on Adam without deformed gradients, no additional radial terms and no radius ratio (abc).

To avoid the ratio $\frac{r_k}{r_i}$ in the effective learning direction and thus to cancel **(c)**, we rescale the momentum in the update by the factor $\frac{r_{k-1}}{r_k}$ at each iteration $k \geq 1$. From Lemma. 1, we obtain:

$$\mathbb{R}(\mathbf{a}_{k-1}) \stackrel{\text{def}}{=} \frac{r_{k-1}}{r_k} \mathbf{a}_{k-1} \quad (72)$$

$$\mathbf{a}_k = \beta \mathbb{R}(\mathbf{a}_{k-1}) + \nabla \mathcal{L}(\mathbf{x}_k) + \lambda \mathbf{x}_k \quad (73)$$

$$= \frac{1}{r_k} \left(\sum_{i=0}^k \beta^{k-i} (\nabla \mathcal{L}(\mathbf{u}_k) + \lambda r_k r_i \mathbf{u}_i) \right). \quad (74)$$

Note that now, the factor $\frac{r_k}{r_i}$ is not contained anymore in the gradient contribution of $\mathbf{c}_k = r_k \mathbf{a}_k$, which neutralizes the radius ratio phenomenon.

We can note that \mathbb{R} and \mathbb{T} are commutative and that we can combine them in a simple concise scalar expression:

$$\mathbb{RT}(\mathbf{a}_{k-1}) \stackrel{\text{def}}{=} \frac{\langle \mathbf{x}_k, \mathbf{x}_{k-1} \rangle \mathbf{a}_{k-1} - \langle \mathbf{x}_k, \mathbf{a}_{k-1} \rangle \mathbf{x}_{k-1}}{\langle \mathbf{x}_k, \mathbf{x}_k \rangle}, \quad (75)$$

$$\mathbf{a}_k = \beta \mathbb{RT}(\mathbf{a}_{k-1}) + \nabla \mathcal{L}(\mathbf{x}_k) + \lambda \mathbf{x}_k. \quad (76)$$

This new momentum leads to $\mathbf{c}_k = \mathbf{c}_k^{\text{RT}} + r_k^2 \lambda \mathbf{u}_k$ with $\langle \mathbf{c}_k, \mathbf{u}_k \rangle = \lambda r_k^2$ and $\mathbf{c}_k^\perp = \mathbf{c}_k^{\text{RT}}$. The latter relies only on the trajectory on the hypersphere and always lies in the tangent space:

$$\mathbf{c}_k^{\text{RT}} = \beta \Gamma_{\mathbf{u}_{k-1}}^{\mathbf{u}_k}(\mathbf{c}_{k-1}^{\text{RT}}) + \nabla \mathcal{L}(\mathbf{u}_k). \quad (77)$$

The final Adam w/o (abc) scheme reads:

$$\mathbf{x}_{k+1} = \mathbf{x}_k - \eta_k \frac{\mathbf{m}_k}{1 - \beta_1^{k+1}} / \sqrt{\frac{v_k}{1 - \beta_2^{k+1}} + \epsilon}, \quad (78)$$

$$\mathbf{m}_k = \beta_1 \text{RT}(\mathbf{m}_{k-1}) + (1 - \beta_1)(\nabla \mathcal{L}(\mathbf{x}_k) + \lambda \mathbf{x}_k), \quad (79)$$

$$v_k = \beta_2 \frac{r_k^2}{r_k^2} v_{k-1} + (1 - \beta_2) d^{-1} \|\nabla \mathcal{L}(\mathbf{x}_k) + \lambda \mathbf{x}_k\|^2. \quad (80)$$

We also rescale the introduced scalar v_k at each step with the factor $\frac{r_k^2}{r_k^2}$. This removes the radius from the gradient contribution of the scheduling $\nu^R = r_k v_k$, in contrast with ν_k from Eq. (43). The new scheduling effect reads:

$$\nu_k^R = d^{-1/2} \frac{1 - \beta_1^{k+1}}{1 - \beta_1} \sqrt{\frac{1 - \beta_2}{1 - \beta_2^{k+1}}} \left(\sum_{i=0}^k \beta_2^{k-i} \|\nabla \mathcal{L}(\mathbf{u}_i) + \lambda r_i \mathbf{u}_i\|^2 \right)^{1/2}.$$

D.3 TRAINING AND IMPLEMENTATION DETAILS

To assess empirically the significance of the above phenomena in the context of CNNs with BN, we evaluate the different variants of AdamW, AdamG, Adam w/o (a), w/o (ab), w/o (abc) over a variety of datasets and architectures.

Note that the set of parameters θ of a CNN with BN layers can be split in two disjoint subsets: $\theta = \mathcal{F} \cup \mathcal{R}$, where \mathcal{F} is the set of groups of radially-invariant parameters and \mathcal{R} the remaining parameters. As demonstrated in Appendix A, the subset \mathcal{F} includes parameters of all filters followed by BN. Since we are only interested in comparing optimization on \mathcal{F} , Adam variants w/o (a), w/o (ab), w/o (abc), AdamW AdamG are applied only to the optimization of the parameters in \mathcal{F} whereas the ones in \mathcal{R} are optimized with the original Adam scheme. The algorithm of Adam w/o (abc) is illustrated in Algorithm 1.

For each optimization scheme, each dataset and each architecture, the same grid search range and budget was performed while mini-batch size was fixed. We used a mini-batch size of 128 for SVHN, CIFAR10 and CIFAR100. The learning rates η varied in $\{10^{-4}, 10^{-3}, 10^{-2}, 10^{-1}\}$, the weight decay in $10^{-3} \cdot \{0, \frac{1}{128}, \frac{1}{64}, \frac{1}{32}, \frac{1}{32}, \frac{1}{16}, \frac{1}{8}, \frac{1}{4}\}$ (similar to Loshchilov & Hutter (2019)), the momentum was fixed to 0.9 (β_1 for variants of Adam) and the order-two moment β_2 in $\{0.99, 0.999, 0.9999\}$ (as in Kingma & Ba (2015)).

We used the same step-wise learning rate scheduler for each method. For SVHN, CIFAR10 and CIFAR100, models were trained for 405 epochs, and the learning rate multiplied by 0.1 at epochs 135, 225 and 315.

The optimization schemes introduced in this paper do not change the complexity in time of the algorithm. During the update of parameters in a layer, we only do a temporary copy of the parameter tensor just before the update to perform the RT transformation. This temporary copy is flushed after the RT transformation. Nothing permanent is stored in the optimizer.

Note that, for each architecture and each dataset, the same learning rate was systematically found for each method while the momentum factor was fixed at 0.9 (cf. Table 3).

Other hyperparameters, e.g., L_2 regularization and order-2 moment, are illustrated in Table 4.

D.4 ADDITIONNAL EMPIRICAL RESULTS

In this section we provide the mean loss training curves associated to Table 2 for every Adam variant.

Table 3: Best learning rate and momentum factor. We systematically found the same learning rate for each dataset and architecture while the momentum factor was fixed to 0.9.

Method	η_0	β, β_1
Adam w/o (a)	0.001	0.9
Adam w/o (ab)	0.001	0.9
Adam w/o (abc)	0.001	0.9
Adam	0.001	0.9
AdamW	0.001	0.9
AdamG	0.01	0.9

Algorithm 1 Adam w/o (abc) and its algorithm illustrated for a filter $\mathbf{x} \in \mathbb{R}^d$ followed by BN. Steps that are different from Adam are shown in highlight. For non-convolutional layers we use standard Adam.

Require: $\beta_1, \beta_2 \in [0, 1)$; $\lambda, \eta \in \mathbb{R}$; $\mathcal{L}(\mathbf{x})$
1: **initialize** step $k \leftarrow -1$; $\mathbf{m}_k \leftarrow 0$; $v_k \leftarrow 0$; $\mathbf{x} \in \mathbb{R}^d$
2: **while** stopping criterion not met **do**
3: $k \leftarrow k + 1$
4: $\mathbf{g} \leftarrow \nabla \mathcal{L}(\mathbf{x}_k) + \lambda \mathbf{x}_k$
5: $\mathbf{m}_k \leftarrow \beta_1 \mathbf{m}_{k-1} + (1 - \beta_1) \mathbf{g}$
6: $v_k \leftarrow \beta_2 v_{k-1} + (1 - \beta_2) d^{-1} \mathbf{g}^\top \mathbf{g}$
7: $\hat{\mathbf{m}} \leftarrow \mathbf{m}_k / (1 - \beta_1^{k+1})$
8: $\hat{v} \leftarrow v_k / (1 - \beta_2^{k+1})$
9: $\mathbf{x}_{k+1} \leftarrow \mathbf{x}_k - \eta \hat{\mathbf{m}} / (\sqrt{\hat{v}} + \epsilon)$
10: $\mathbf{m}_k \leftarrow \mathbf{m}_k (\mathbf{x}_{k+1}^\top \mathbf{x}_k \mathbf{m}_k - \mathbf{m}_k^\top \mathbf{x}_{k+1} \mathbf{x}_k) / (\mathbf{x}_{k+1}^\top \mathbf{x}_{k+1})$
11: $v_k \leftarrow v_k (\mathbf{x}_k^\top \mathbf{x}_k / \mathbf{x}_{k+1}^\top \mathbf{x}_{k+1})$
12: **return** resulting parameters \mathbf{x}_k

Table 4: Best L_2 regularization (λ) and order-2 moment factors (β_2).

Setup		Adam	AdamW	AdamG	Adam w/o (a)	Adam w/o (ab)	Adam w/o (abc)
ResNet20	λ	0.000250	0.000500	0.000125	0.000031	0.00125	0.000500
	β_2	0.99	0.99	0.99	0.99	0.99	0.99
CIFAR10	λ	0.000250	0.000008	0.000063	0.000250	0.00125	0.000016
	β_2	0.999	0.99	0.99	0.99	0.99	0.99
VGG16	λ	0.000250	0.000031	0.000250	0.000063	0.0	0.000031
	β_2	0.999	0.999	0.999	0.999	0.99	0.999
CIFAR100	λ	0.000125	0.000125	0.000125	0.000125	0.00125	0.0
	β_2	0.999	0.99	0.99	0.99	0.99	0.999
VGG16	λ	0.000063	0.000016	0.000063	0.000063	0.00125	0.000008
	β_2	0.99	0.99	0.99	0.99	0.99	0.99
SVHN	λ	0.0	0.000008	0.000500	0.000031	0.0005	0.000008
	β_2	0.999	0.999	0.99	0.99	0.999	0.999
VGG16	λ	0.0	0.000031	0.000500	0.000008	0.00025,	0.000250
	β_2	0.99	0.99	0.99	0.99	0.99	0.999

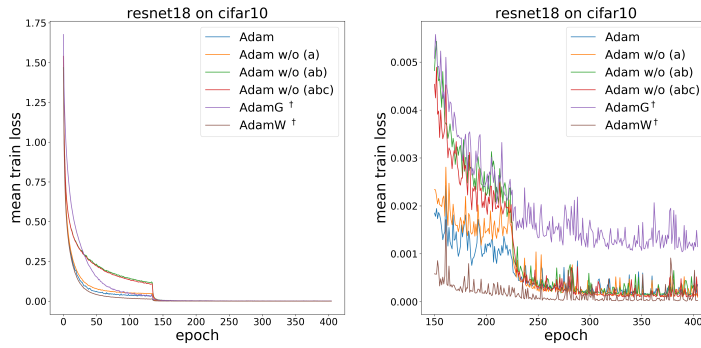


Figure 7: Training speed comparison with ResNet18 on CIFAR10. *Left:* Mean training loss over all training epochs (averaged across 5 seeds) for different Adam variants. *Right:* Zoom-in on the last epochs. Please refer to Table 2 for the corresponding accuracies.

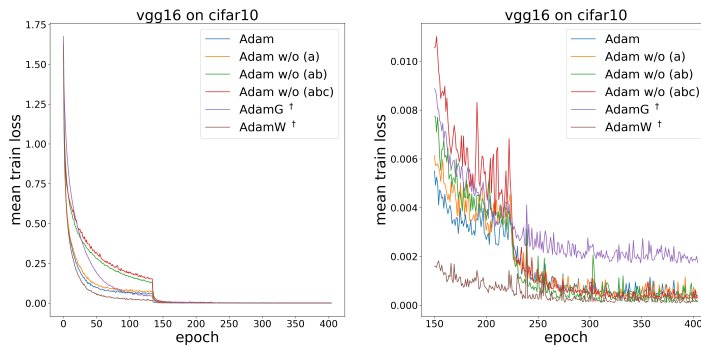


Figure 8: Training speed comparison with VGG16 on CIFAR10. *Left:* Mean training loss over all training epochs (averaged across 5 seeds) for different Adam variants. *Right:* Zoom-in on the last epochs. Please refer to Table 2 for the corresponding accuracies.

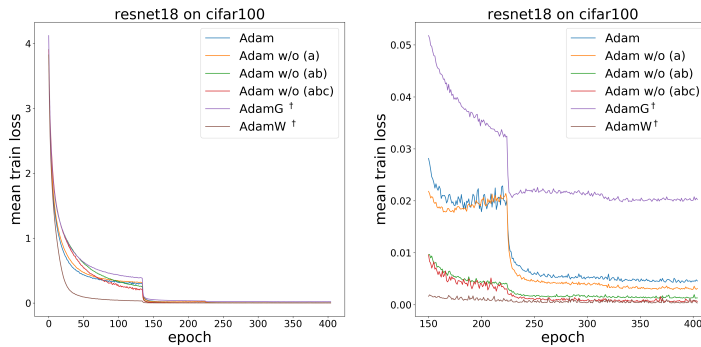


Figure 9: Training speed comparison with ResNet18 on CIFAR100. *Left:* Mean training loss over all training epochs (averaged across 5 seeds) for different Adam variants. *Right:* Zoom-in on the last epochs. Please refer to Table 2 for the corresponding accuracies.

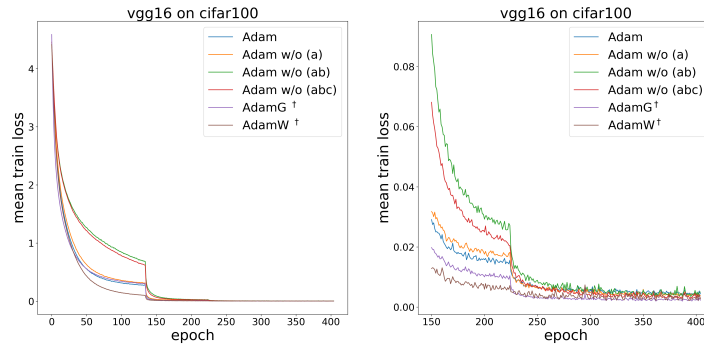


Figure 10: Training speed comparison with VGG16 on CIFAR100. *Left:* Mean training loss over all training epochs (averaged across 5 seeds) for different Adam variants. *Right:* Zoom-in on the last epochs. Please refer to Table 2 for the corresponding accuracies.

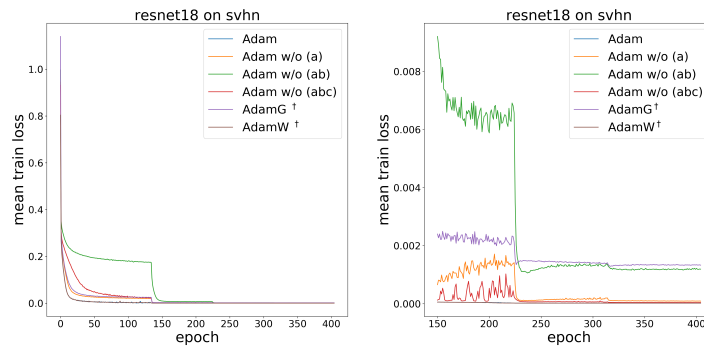


Figure 11: Training speed comparison with ResNet18 on SVHN. *Left:* Mean training loss over all training epochs (averaged across 5 seeds) for different Adam variants. *Right:* Zoom-in on the last epochs. Please refer to Table 2 for the corresponding accuracies.

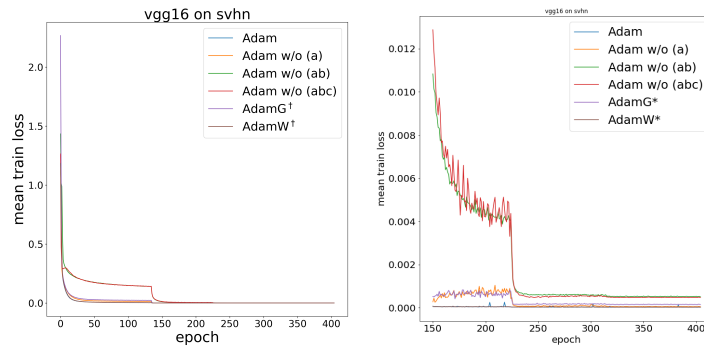


Figure 12: Training speed comparison with VGG16 on SVHN. *Left:* Mean training loss over all training epochs (averaged across 5 seeds) for different Adam variants. *Right:* Zoom-in on the last epochs. Please refer to Table 2 for the corresponding accuracies.